

IMPERIAL COLLEGE LONDON

DEPARTMENT OF ELECTRICAL AND ELECTRONIC ENGINEERING

Signal Optimization for Wireless Information and Power Transmission

Author:

Yang Zhao
(CID: 01561245)

Supervisor:

Dr Bruno Clerckx

Co-Supervisor:

Dr Morteza Varasteh

A thesis submitted for the degree of

MSc Communications and Signal Processing

September 2, 2019

Contents

1	Introduction	4
1.1	Background	4
1.2	Literature Review	4
1.3	Objectives and Methodology	5
2	From WPT to WIPT	6
2.1	WPT Architecture	6
2.2	Rectenna Design	7
2.2.1	Rectenna Behavior	7
2.2.2	Antenna Model	8
2.3	Diode Characteristics	9
2.4	Receiver Architectures	11
2.4.1	Time Switching	11
2.4.2	Power Splitting	11
2.5	Signal and System Model	12
2.5.1	Transmitted Information Waveform	12
2.5.2	Transmitted Power Waveform	13
2.5.3	Multipath Channel and Received Signal	14
2.6	Information Decoder	15
2.7	Energy Harvester	15
3	Rate-Energy Tradeoff	18
3.1	Rate-Energy Region Characterization	18
3.2	Problem Formulation	18
3.3	Decoupled Design	21
3.4	Twofold Benefit of Superposed Waveform	23
3.5	PAPR Constraints	25
3.6	Multiple Rectennas	26
4	Performance Evaluation	29
4.1	SISO	29
4.1.1	R-E Region vs Subband	30
4.1.2	R-E Region vs SNR	32
4.1.3	R-E Region vs PAPR	34
4.2	MISO	35
4.3	MIMO	36

List of Figures

2.1	Block diagram of a conventional far-field WPT architecture [1]	6
2.2	Comparison of a typical 3-subcarrier multisine and CW in time and frequency domains (modified from [2])	8
2.3	Rectenna architecture	8
2.4	Structure of time switching receiver [3]	11
2.5	Structure of power splitting receiver [3]	12
4.1	Frequency response of the SISO FF and FS channels	30
4.2	R-E region vs N for FF and FS channels	31
4.3	Optimal R-E region for FF channel with medium N	32
4.4	R-E region vs SNR for FF channel	33
4.5	R-E region vs SNR for FS channel	34
4.6	R-E region vs PAPR for FF channel	35
4.7	R-E region vs M over FF channel: an instance and the average over 100 realizations	36
4.8	Rate and current CDF vs M for MISO FF channels	37
4.9	Frequency response of the MIMO FF channel	38
4.10	R-E region vs N and U for MIMO FF channels	38

List of Tables

4.1	Reference parameters used in the simulation	29
-----	---	----

Chapter 1

Introduction

1.1 Background

Energy-constrained wireless devices are conventionally powered by batteries. However, the development of large-scale networks as Internet-of-Things (IoT) is strictly restricted by its limited working time and frequent recharging or replacement. Although Wireless Power Transfer (WPT) via inductive coupling has enjoyed some success in real-world applications, it is impractical for most devices on the move since the operation range is very short. As a promising alternative, the Radio-Frequency (RF) wave is typically with lower power level (μW to W) but larger coverage (up to hundreds of meters) [4]. Interestingly, it indeed carries both information and energy simultaneously, with the potential to power billions of mobile nodes wirelessly while keeping them connected. The recent revolution in harvester model and the significant power drop of electronics bring more possibility to the research on Wireless Information and Power Transfer (WIPT) via RF signals.

1.2 Literature Review

Significant improvements on WIPT has been witnessed in the last decade. The idea was first proposed in [5], where the author first defined a nonlinear concave capacity-energy function and investigated the tradeoff for typical binary channels and a flat additive white Gaussian noise (AWGN) channel with amplitude-constrained inputs. It was extended to frequency-selective channel in [6]. However, both works were based on the impractical assumption that information decoding (ID) and Energy Harvesting (EH) can be performed individually on the same received signal. In [7], the authors proposed two practical co-located receiver designs named *time switching* (TS) that switches between ID and EH and *power splitting* (PS) that splits the received power into two separate streams. It was then demonstrated in [8] that TS can guarantee the same rate as conventional Time-Division Multiple Access (TDMA) while providing considerable power. In comparison, PS may lead to higher rate when the demand on power is sufficiently high. A further research [9] enabled dynamic power splitting that adjusts the power split ratio based on the channel state information (CSI), and proposed a suboptimal low-complexity *antenna switching* scheme. Nevertheless, the literatures above are mostly based on an oversimplified linear harvester model. To accurately characterize the behavior of the rectenna, [10] derived a tractable nonlinear model and performed an adap-

tive multisine waveform design accordingly. Realistic simulations showed significant gains in harvested power and stressed the importance of modelling rectifier non-linearity in wireless system design. The work was extended to multi-input single-output (MISO) WIPT in [11] where a superposition of multicarrier modulated and unmodulated waveform was optimized as a function of CSI under transmit power budget. It suggested the rectifier nonlinearity can lead to a larger rate-energy (R-E) region and favours a different waveform, modulation and input distribution. In another perspective, a learning approach [12] modelled the transmitter and receiver as deep neural networks (NN) and jointly optimized signal encoding with network parameters. Constellations showed that the offset of the power symbol is positively correlated to the power demand, while the information symbols are symmetrically located around the origin. The pattern confirmed a unmodulated waveform is beneficial to increase the harvested power.

1.3 Objectives and Methodology

In this article, we depart from the rectifier behavior and diode characteristics to revisit the analytical harvester models proposed in [10]. On top of this, a multi-carrier modulated waveform and a multi-carrier unmodulated waveform are compared in terms of harvested energy. The results demonstrated that when considering rectifier nonlinearity, the unmodulated waveform outperforms the modulated waveform for multi-carrier WPT but is outperformed for single-carrier transmission. It is in sharp contrast to the conventional opinion based on linear rectifier model.

We also explore the adaptive transceiver design in [11] that jointly optimizes the superposed signal (consists of modulated and unmodulated components) at the transmitter and the power splitter at the receiver. The characterization of the R-E region is converted into an optimization problem maximizing the harvested current with discrete rate constraints, which relies on Geometric Programming (GP) tools. The original strategy for Multiple-Input Single-Output (MISO) is extended to Multiple-Input Multiple-Output (MIMO), and the Peak-to-Average Power Ratio (PAPR) constraint is introduced to the system.

Chapter 2

From WPT to WIPT

In this section, we first introduce a general WPT architecture. Next, we focus on the rectenna behavior and derive the analytical diode models for the energy harvester. We then extend the work to WIPT and explore two practical receiver structures. Finally, the signal and system model is established, and the dependency of delivered power on signal design is investigated on top of it.

2.1 WPT Architecture

According to the operation principle, WPT systems can be categorized as *maximum power transfer* that maximizes the coverage and *maximum energy efficiency transfer* [13] that compromise with the power budget. Figure 2.1 illustrates the fundamental blocks of a generic WPT system.

The transmit power efficiency e is decomposed as:

$$e = \frac{P_{\text{dc,ST}}}{P_{\text{dc}}^t} = \underbrace{\frac{P_{\text{rf}}^t}{P_{\text{dc}}^t}}_{e_1} \cdot \underbrace{\frac{P_{\text{rf}}^r}{P_{\text{rf}}^t}}_{e_2} \cdot \underbrace{\frac{P_{\text{dc}}^r}{P_{\text{rf}}^r}}_{e_3} \cdot \underbrace{\frac{P_{\text{dc,ST}}}{P_{\text{dc}}^r}}_{e_4} \quad (2.1)$$

Most existing solutions assumed no dependency for the components and focused on maximizing each term individually. Nevertheless, it has been proved by [14, 10, 15] that these efficiencies are indeed coupled with each other, especially when input power is not very high (below 1 mW). Specifically, the DC-to-RF efficiency e_1 is related to the Peak-to-Average Power Ratio (PAPR) hence the waveform [16]. Similarly, the RF-to-RF efficiency e_2 is determined by the channel state and the signal characteristics as waveform, beamformer, modulation, and power allocation [3]. It also desires a highly directional transmission [17]. e_3 measures the RF-to-DC efficiency of the rectenna, which relates to the rectifier input power P_{rf}^r [2, 18, 1],

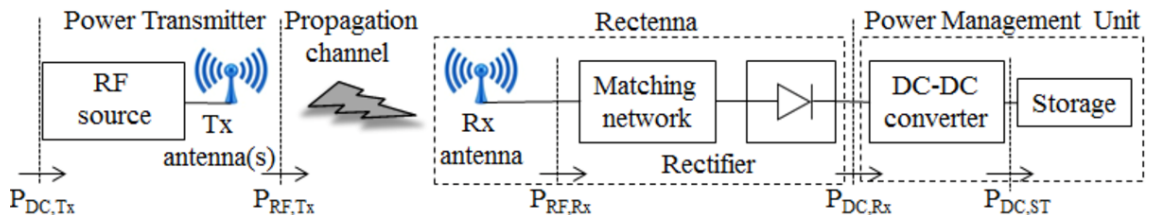


Figure 2.1: Block diagram of a conventional far-field WPT architecture [1]

channel and the transmit signal [19, 20, 3]. Finally, the DC-to-DC efficiency e_4 can be maximized by dynamically adjusting the rectifier load with the diode impedance [21]. Therefore, we desire a flexible transmitter to optimize the signal adaptively over CSI to maximize the power transfer efficiency e .

From the perspective of WPT, this article particularly investigates the relationship between signal design and $e_2 \cdot e_3$ based on the nonlinear harvester model proposed in [10].

2.2 Rectenna Design

2.2.1 Rectenna Behavior

A rectenna receives electromagnetic power with antenna and convert it to electric power with rectifier. Diverse configurations are available for energy harvesting, such as *Schottky* [22, 23], *CMOS* [24, 25], *series* [26, 27], *shunt* [28, 29]. Interestingly, those models are not equally suitable for the same input power, and maximizing the rectenna efficiency e_3 requires a proper selection according to the power range. As reported in [25, 30], low barrier Schottky diodes are commonly used for input power between 1 μ W and 1 mW. Specifically, single diode is preferred for low power below 500 μ W and multiple diodes are typically applied for input power above 500 μ W [3]. Hybrid designs as [31] may be employed to maintain a high efficiency for large power range.

Besides the rectenna model, the shape of the received signal also influences the RF-to-DC efficiency e_3 . It was first demonstrated in [2] that multisine waveform *i.e.* *Power-Optimized waveform (POW)* outperforms the single tone waveform *i.e.* *Continuous Wave (CW)* in operation range and power efficiency. The expression of a multisine waveform with N subcarriers writes as a summation of N sine waves:

$$V_{\text{multisine}}(t) = \sum_{n=0}^{N-1} \frac{1}{\sqrt{N}} \sin(2\pi(f_0 + n\Delta f)t) \quad (2.2)$$

where f_0 is the minimum frequency and Δf is the spacing. Figure 2.2 [2] illustrates the three-subcarrier case for both signals in time and frequency domains. It can be observed that multisine waveform provides a higher PAPR equals to \sqrt{N} and occupies a bandwidth of $(N - 1)\Delta f$ with the same average power as CW, which is equally distributed to its components. The thick lines indicate examples of rectifier output voltage.

The advantage of multisine in WPT is that the high PAPR increases the peak rectifier output voltage. With a proper signal and circuit design, high voltage may be preserved during the cycle if discharging is slow enough, as indicated by the thick blue line in Figure 2.2(b). To enhance the harvested power, a large number of tones may be used to increase PAPR, and the multisine signal will appear as pulses with period of $1/\Delta f$. Most of the signal power will be concentrated in those pulses to trigger the diode and charge the capacitor. However, more subbands can lead to smaller frequency gaps and longer charging cycle when the bandwidth is fixed.

It can be hard to derive an accurate expression of the RF-to-DC efficiency e_3 on the power and shape of the rectifier input signal, as practical energy harvesting circuits consists of various nonlinear components as diodes, capacitors and inductors.

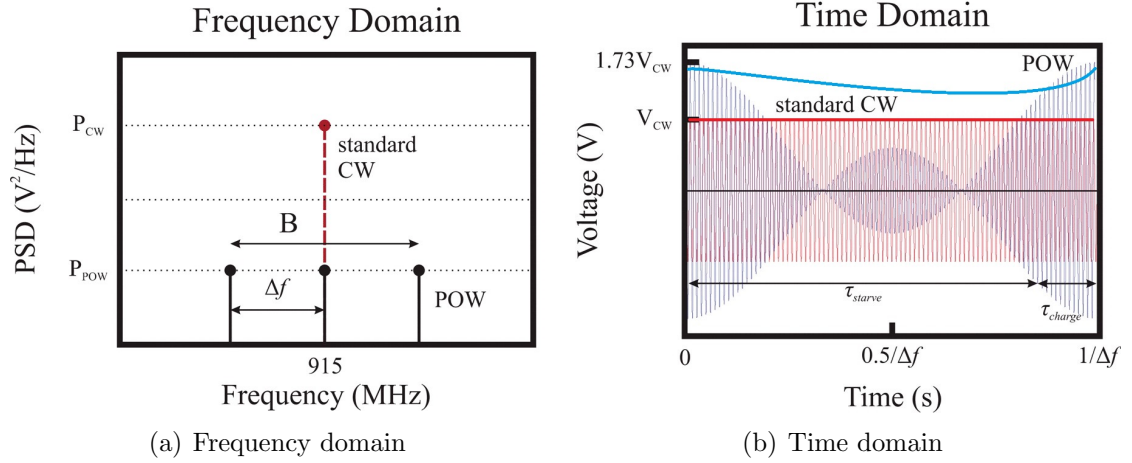


Figure 2.2: Comparison of a typical 3-subcarrier multisine and CW in time and frequency domains (modified from [2])

It is also sensitive to parasitic sources, impedance matching, and harmonic generation [32, 25]. In this article, we employ the *diode linear model* and *diode nonlinear model* proposed in [10] based on the diode current-voltage (I-V) characteristics to capture the fundamental pattern of rectenna and investigate its impact on resource allocation and system design. A superposed waveform containing modulated information and multisine power components is optimized according to CSI on top of both models.

2.2.2 Antenna Model

As illustrated by Figure 2.3(b), the rectifier consists of a single diode as the source of nonlinearity and a low-pass filter to store energy.

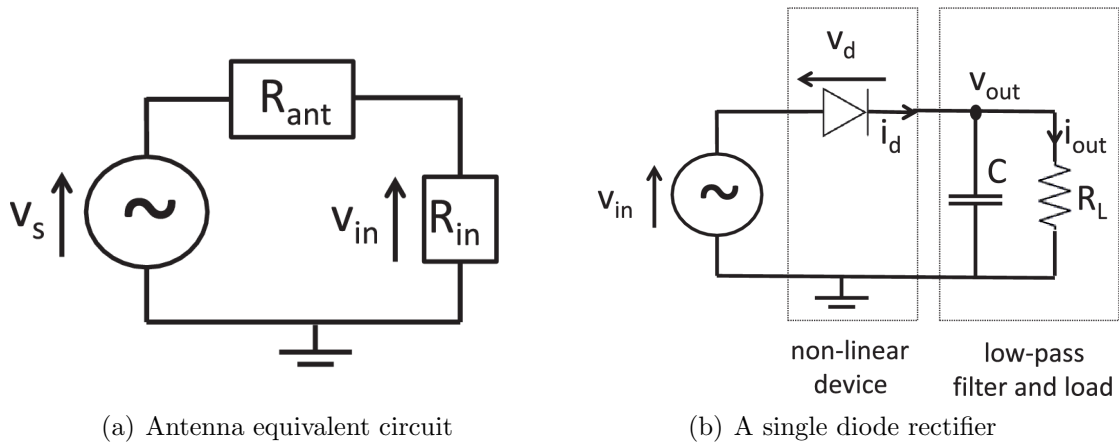


Figure 2.3: Rectenna architecture

Figure 2.3(a) shows that the antenna equivalent circuit includes a voltage source $v_s(t)$ connected to a series antenna impedance $Z_{\text{ant}} = R_{\text{ant}} + jX_{\text{ant}}$ followed by a combined impedance of the rectifier and the matching network $Z_{\text{in}} = R_{\text{in}} + jX_{\text{in}}$. Assuming lossless, the perfect matching condition is

$$R_{\text{in}} = R_{\text{ant}}, X_{\text{in}} = -X_{\text{ant}} \quad (2.3)$$

When equation 2.3 is satisfied, the rectifier input voltage equals

$$v_{\text{in}}(t) = v_s(t)/2 = y(t)\sqrt{R_{\text{in}}} \quad (2.4)$$

where $y(t)$ is the received signal. Therefore, the input power to the rectifier writes

$$P_{\text{rf}}^r = \mathbb{E}[y(t)^2] = \mathbb{E}[v_{\text{in}}(t)^2] / R_{\text{in}} \quad (2.5)$$

It is also assumed that the noise is too small to be harvested.

2.3 Diode Characteristics

Consider the single diode rectifier presented in Figure 2.3(b) for simplicity. Without loss of generality, the employed diode models hold for general circuits as voltage doubler and bridge rectifiers [33].

Denote $v_{\text{in}}(t)$ and $v_{\text{out}}(t)$ as diode input and output voltages, the voltage across the diode is $v_{\text{d}}(t) = v_{\text{in}}(t) - v_{\text{out}}(t)$. It determines the current flowing through the diode:

$$i_{\text{d}}(t) = i_{\text{s}} \left(e^{\frac{v_{\text{d}}(t)}{nv_{\text{t}}}} - 1 \right) \quad (2.6)$$

where i_{s} is the reverse saturation current, n is the ideality factor, and v_{t} is the thermal voltage. With a Taylor series expansion around a quiescent point $a = v_{\text{d}}(t)$, equation 2.6 rewrites as:

$$i_{\text{d}}(t) = \sum_{i=0}^{\infty} k'_i (v_{\text{d}}(t) - a)^i \quad (2.7)$$

where

$$k'_i = \begin{cases} i_{\text{s}} \left(e^{\frac{a}{nv_{\text{t}}}} - 1 \right), & i = 0 \\ i_{\text{s}} \frac{e^{\frac{a}{nv_{\text{t}}}}}{i!(nv_{\text{t}})^i}, & i \in \mathbb{N}^+ \end{cases} \quad (2.8)$$

k'_i relates to the diode parameters and is a constant when a is fixed. Note that the Taylor series expression is a small-signal model that only fits for the nonlinear operation region of the diode. Therefore, equation 2.7 is no longer accurate for a large input voltage $v_{\text{in}}(t)$, where the diode behavior is dominated by the series resistor and the I-V relationship is linear [23].

Also, we assume an ideal rectifier with steady-state response that delivers a constant output voltage v_{out} , whose amplitude is only a function of the peaks of the input voltage $v_{\text{in}}(t)$ [34]. Based on the assumptions, a proper choice of voltage drop would be

$$a = \mathbb{E}[v_{\text{d}}(t)] = \mathbb{E}[v_{\text{in}}(t) - v_{\text{out}}] = -v_{\text{out}} \quad (2.9)$$

as

$$\mathbb{E}[v_{\text{in}}(t)] = \sqrt{R_{\text{ant}}} \mathbb{E}[y(t)] = 0 \quad (2.10)$$

On top of equation 2.9 and 2.4, the diode current in 2.7 can be expressed as

$$i_{\text{d}}(t) = \sum_{i=0}^{\infty} k'_i v_{\text{in}}(t)^i = \sum_{i=0}^{\infty} k'_i R_{\text{ant}}^{i/2} y(t)^i \quad (2.11)$$

Equation 2.11 reveals an explicit relationship between the received waveform $y(t)$ and the diode current $i_{\text{d}}(t)$. Nevertheless, as the signal carries both power and information simultaneously, the waveform varies at every symbol period due to the randomness of modulation. Hence, the diode current $i_{\text{d}}(t)$ fluctuates with time as well. By taking an expectation over the symbol distribution, the harvested DC current can be modelled as

$$i_{\text{out}} = \mathbb{E}[i_{\text{d}}(t)] \quad (2.12)$$

and the available power is

$$P_{\text{dc}}^r = i_{\text{out}}^2 R_{\text{L}} \quad (2.13)$$

To investigate the fundamental dependency of harvested power on waveform design, a practical strategy is to approximate equation 2.11 with a truncation to the n_o -th order:

$$i_{\text{out}} \approx \sum_{i=0}^{n_o} k'_i R_{\text{ant}}^{i/2} \mathbb{E}[y(t)^i] \quad (2.14)$$

The contribution of odd terms is indeed zero, as $\mathbb{E}[y(t)^i] = 0$ for odd i . Therefore, we only need to consider the even terms, and the approximated rectifier output DC current is:

$$i_{\text{out}} \approx \sum_{i \text{ even}, i \geq 0}^{n_o} k'_i R_{\text{ant}}^{i/2} \mathbb{E}[y(t)^i] \quad (2.15)$$

Recall from equation 2.8 that the diode parameter k'_i is a function of $a = -v_{\text{out}}$ and relates to the output current as well. Therefore, equation 2.41 is actually

$$i_{\text{out}} \approx \sum_{i \text{ even}, i \geq 0}^{n_o} k'_i(i_{\text{out}}) R_{\text{ant}}^{i/2} \mathbb{E}[y(t)^i] \quad (2.16)$$

Following [10], we denote

$$k''_0 = e^{\frac{a}{nv_t}} = e^{-\frac{R_{\text{L}} i_{\text{out}}}{nv_t}} \quad (2.17)$$

Hence, $k'_0 = i_{\text{s}}(k''_0 - 1)$ and 2.16 rewrites as

$$e^{\frac{R_{\text{L}} i_{\text{out}}}{nv_t}} (i_{\text{out}} + i_{\text{s}}) \approx i_{\text{s}} + \sum_{i \text{ even}, i \geq 2}^{n_o} \frac{k'_i}{k''_0} R_{\text{ant}}^{i/2} \mathbb{E}[y(t)^i] \quad (2.18)$$

Further, denote

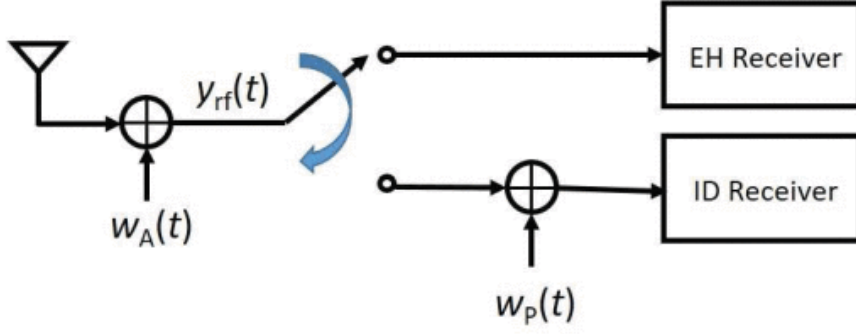


Figure 2.4: Structure of time switching receiver [3]

$$k_i = \frac{k'_i}{k''_0} = \frac{i_s}{i!(nv_t)^i} \quad (2.19)$$

Note the r.h.s. of equation 2.18 depends on k_i and is independent of i_{out} . On the other hand, the l.h.s. is a monotonic increasing function of i_{out} . Therefore, maximizing i_{out} is equivalent to maximizing the target function

$$z_{DC} = \sum_{i \text{ even}, i \geq 2}^{n_o} k_i R_{\text{ant}}^{i/2} \mathbb{E} [y(t)^i] \quad (2.20)$$

2.4 Receiver Architectures

We investigated two practical architectures for the co-located integrated information and energy receiver. Both designs are equipped with individual ID and EH receivers. The former is a conventional baseband demodulator while the latter can be realized with the proposed rectifier structure in Section 2.2.

2.4.1 Time Switching

A *Time Switching (TS)* receiver (Figure 2.4) operates as either an information decoder or an energy harvester at a certain time. In the design, the transmitter divides the transmission block into orthogonal power and data slots with length ratio α and $1 - \alpha$ respectively, then optimizes the waveform for WPT or WIT individually. Also, the receiver periodically switches between ID and EH receivers in the corresponding slots. We assume perfect synchronization between transmitter and receiver for mode control. It can achieve different rate-energy tradeoffs by adjusting the slot length ratio α jointly with the transmit signals. As the input power range for information and power receivers are typically different, TS can be combined with a "near-far" scheduling [7] to benefit the system efficiency.

2.4.2 Power Splitting

In a *Power Splitting (PS)* receiver (Figure 2.5), we introduce a PS ratio ρ to split the received signal into separate power stream (with proportion ρ) and information stream (with proportion $1 - \rho$). At the transmitter, the signal is jointly optimized

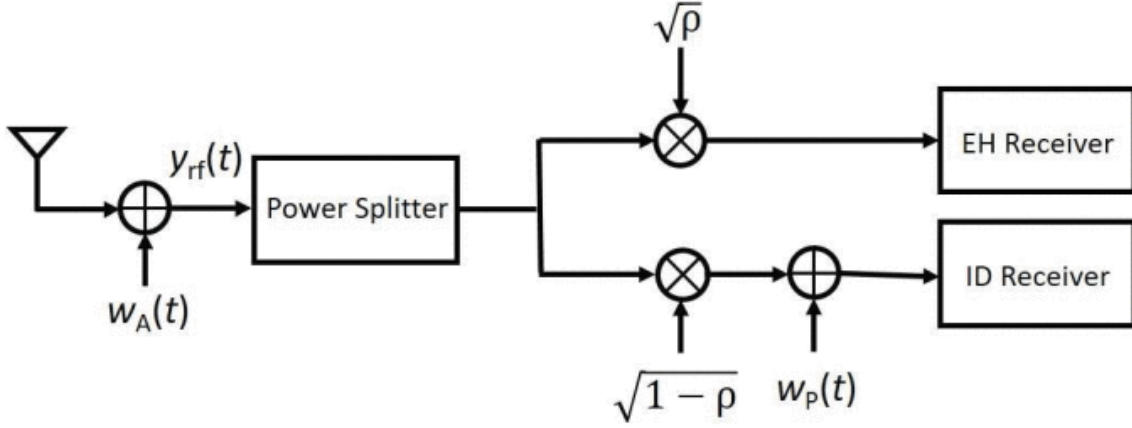


Figure 2.5: Structure of power splitting receiver [3]

for information and power transmission according to CSIT. With the assumption of perfect matching, the EH and ID receivers are with input voltage signals $\sqrt{\rho R_{\text{ant}}}y(t)$ and $\sqrt{(1-\rho)R_{\text{ant}}}y(t)$ respectively. Varying the PS ratio ρ and the transmit signals leads to different rate-energy points. It is argued in [7] that the PS scheme is optimal for ideal RF-to-baseband signal conversion with negligible processing noise, but the condition is hard to meet in practice.

2.5 Signal and System Model

Consider a point-to-point MISO WIPT system in multipath environment. The M -antenna transmitter delivers information and power simultaneously to the single-antenna receiver through N orthogonal subbands. It is assumed the carrier frequencies are with even spacing Δf and equal bandwidth B_s . The n -th subband has carrier frequency $f_n = f_0 + n\Delta f$ for $n = 0, \dots, N-1$. To maximize the rate-energy tradeoff, we employ a superposed signal consists of a multi-carrier deterministic multisine waveform and a multi-carrier random modulated waveform for WIPT. Both components are transmitted on the same frequency bands.

2.5.1 Transmitted Information Waveform

Denote the information symbol carried by the modulated waveform on subband n as \tilde{x}_n , we assume the input symbol is with the capacity-achieving i.i.d. Circular Symmetric Complex Gaussian (CSCG) distribution with zero mean and unit variance [35]:

$$\tilde{x}_n = |\tilde{x}_n| e^{j\phi_{\tilde{x}_n}} \sim \mathcal{CN}(0, 1) \quad (2.21)$$

Hence, the modulated waveform on antenna $m = 1, \dots, M$, subband n writes as

$$x_{n,m} = w_{I,n,m} \tilde{x}_n \quad (2.22)$$

where $w_{I,n,m}$ is the corresponding information weight and is a constant for a certain channel state:

$$w_{I,n,m} = |w_{I,n,m}| e^{j\phi_{I,n,m}} = s_{I,n,m} e^{j\phi_{I,n,m}} \quad (2.23)$$

Note the amplitude and phase are separated in resource allocation. Define matrices \mathbf{S}_I and $\mathbf{\Phi}_I$ of size $N \times M$ such that the (n, m) entries hold $s_{I,n,m}$ and $\phi_{I,n,m}$ respectively, the design of information waveform is converted into an optimization problem on both matrices, with the average WIT transmit power $P_I = \frac{1}{2} \|\mathbf{S}_I\|_F^2$. The modulated symbol of equation 2.22 can be further expressed as

$$x_{n,m} = s_{I,n,m} e^{j\phi_{I,n,m}} \cdot |\tilde{x}_n| e^{j\phi_{\tilde{x}_n}} = \tilde{s}_{I,n,m} e^{j\tilde{\phi}_{I,n,m}} \quad (2.24)$$

with $\tilde{s}_{I,n,m} = s_{I,n,m} |\tilde{x}_n|$ and $\tilde{\phi}_{I,n,m} = \phi_{I,n,m} + \phi_{\tilde{x}_n}$. In this way, the impact of symbol distribution and waveform design are combined. The modulated waveform also follows an i.i.d. CSCG distribution with variance equal to the subband power $x_{n,m} \sim \mathcal{CN}(0, s_{I,n,m}^2)$.

Therefore, the information waveform $x_{I,m}(t)$ on antenna m at time t writes as

$$x_{I,m}(t) = \sum_{n=0}^{N-1} \tilde{s}_{I,n,m}(t) \cos(2\pi f_n t + \tilde{\phi}_{I,n,m}(t)) \quad (2.25)$$

$$= \Re \left\{ \sum_{n=0}^{N-1} x_{n,m}(t) e^{j2\pi f_n t} \right\} \quad (2.26)$$

$$= \Re \left\{ \sum_{n=0}^{N-1} w_{I,n,m} \tilde{x}_n(t) e^{j2\pi f_n t} \right\} \quad (2.27)$$

On top of this, the WIT signal vector is spread over M antennas

$$\mathbf{x}_I(t) = \Re \left\{ \sum_{n=0}^{N-1} \mathbf{w}_{I,n} \tilde{x}_n(t) e^{j2\pi f_n t} \right\} \quad (2.28)$$

where $\mathbf{w}_{I,n} = [w_{I,n,1} \cdots w_{I,n,M}]^T$.

2.5.2 Transmitted Power Waveform

Comparing with the information component, the multisine power component is unmodulated and deterministic, so there is no dependency on the distribution of input symbol $\tilde{x}_n(t)$. The power waveform on antenna m , subband n is given by

$$w_{P,n,m} = s_{P,n,m} e^{j\phi_{P,n,m}} \quad (2.29)$$

where $s_{P,n,m}$ and $\phi_{P,n,m}$ are the amplitude and phase of the multisine signal. Collect them into the (n, m) entries of matrices \mathbf{S}_P and $\mathbf{\Phi}_P$, the average power of the WPT waveform is $\frac{1}{2} \|\mathbf{S}_P\|_F^2$. Similarly, the power waveform $x_{P,m}(t)$ on antenna m at time t is

$$x_{P,m}(t) = \sum_{n=0}^{N-1} s_{P,n,m} \cos(2\pi f_n t + \phi_{P,n,m}) \quad (2.30)$$

$$= \Re \left\{ \sum_{n=0}^{N-1} w_{P,n,m} e^{j2\pi f_n t} \right\} \quad (2.31)$$

Combine the power signals on all M antennas, the WPT signal vector writes as

$$\mathbf{x}_P(t) = \Re \left\{ \sum_{n=0}^{N-1} \mathbf{w}_{P,n} e^{j2\pi f_n t} \right\} \quad (2.32)$$

with $\mathbf{w}_{P,n} = [w_{P,n,1} \cdots w_{P,n,M}]^T$.

2.5.3 Multipath Channel and Received Signal

Consider a multipath channel with L paths. For the l -th path ($l = 1, \dots, L$), denote the phase shift between the receive antenna and transmit antenna m of subband n as $\zeta_{n,m,l}$. Let τ_l and α_l be the delay and magnitude gain, and indicate the transmit signal on subband n of antenna m as

$$v_{n,m}(t) = w_{P,n,m} + w_{I,n,m} \tilde{x}_n(t) \quad (2.33)$$

The superposed signal containing modulated information waveform and multi-sine power waveform is demonstrated to bring a two-fold benefit on rate and energy [3]. Also, the channel frequency response is expressed as

$$h_{n,m} = \sum_{l=0}^{L-1} \alpha_l e^{j(-2\pi f_n \tau_l + \zeta_{n,m,l})} = A_{n,m} e^{j\bar{\psi}_{n,m}} \quad (2.34)$$

To ensure $v_{n,m}(t)$ and $\tilde{x}_n(t)$ being narrowband signals, we assume $\max_{l \neq l'} |\tau_l - \tau_{l'}| \ll 1/B_s$. It is also supposed that $v_{n,m}(t - \tau_l) = v_{n,m}(t)$ and $\tilde{x}_n(t - \tau_l) = \tilde{x}_n(t)$. The received signal corresponding to transmit antenna m contains the power component $y_{P,m}(t)$ and the information component $y_{I,m}(t)$

$$y_m(t) = y_{P,m}(t) + y_{I,m}(t) \quad (2.35)$$

$$= \Re \left\{ \sum_{l=0}^{L-1} \sum_{n=0}^{N-1} \alpha_l v_{n,m}(t - \tau_l) e^{j2\pi f_n(t - \tau_l) + \zeta_{n,m,l}} \right\} \quad (2.36)$$

$$\approx \Re \left\{ \sum_{n=0}^{N-1} h_{n,m} v_{n,m}(t) e^{j2\pi f_n t} \right\} \quad (2.37)$$

Hence, the total received signal can be obtained by stacking up equation 2.35 over all transmit signals

$$y(t) = y_P(t) + y_I(t) \quad (2.38)$$

$$= \Re \left\{ \sum_{n=0}^{N-1} \mathbf{h}_n (\mathbf{w}_{P,n} + \mathbf{w}_{I,n} \tilde{x}_n) e^{j2\pi f_n t} \right\} \quad (2.39)$$

where the channel vector is defined as $\mathbf{h}_n = [h_{n,1} \dots h_{n,M}]$.

2.6 Information Decoder

In the superposed transmit signal $x_m(t)$, the modulated component $x_{I,m}(t)$ carries all the information while the multisine component $x_{P,m}(t)$ completely serves the power. Since the latter is deterministic, it creates no interference and has zero contribution to the different entropy of $x_m(t)$ in terms of translation. Therefore, the achievable rate is equal to

$$I(\mathbf{S}_I, \mathbf{\Phi}_I, \rho) = \sum_{n=0}^{N-1} \log_2 \left(1 + \frac{(1-\rho)|\mathbf{h}_n \mathbf{w}_{I,n}|^2}{\sigma_n^2} \right) \quad (2.40)$$

where σ_n^2 is the total variance of the Gaussian noise at the RF-band and the noise introduced during the RF-to-baseband conversion (assumed Gaussian) on tone n . It reaches the maximum rate $I(\mathbf{S}_I^*, \mathbf{\Phi}_I^*, 0)$ and boils down to WIT by setting $\rho = 0$ then performing Maximum Ratio Transmission (MRT) and Water-Filling (WF) power allocation on subbands.

An significant conclusion in [11] is that the rate 2.40 is always achievable with and without waveform cancellation. As the multisine is deterministic, it can either be subtracted from the baseband signal or used to construct the translated codebook. Conventional demodulation can be performed then.

2.7 Energy Harvester

To investigate the impact of the proposed waveform on the harvested power, we apply the received signal expression 2.35 to the diode current equation 2.15.

First, we consider the multicarrier multisine waveform $y_P(t)$. The approximated harvester DC current with multisine excitation writes as

$$i_{\text{out}} \approx k'_0 + \sum_{\substack{i \text{ even} \\ i \geq 2}}^{n_o} k'_i \rho^{i/2} R_{\text{ant}}^{i/2} \mathbb{E} [y_P(t)^i] \quad (2.41)$$

Also, it is derived in [10] that the expectation of the received power waveform to the second and fourth orders write respectively as

$$\mathbb{E} [y_P(t)^2] = \frac{1}{2} \sum_{n=0}^{N-1} |\mathbf{h}_n \mathbf{w}_{P,n}|^2 \quad (2.42)$$

$$= \frac{1}{2} \sum_{n=0}^{N-1} \sum_{m_0, m_1} s_{P,n,m_0} s_{P,n,m_1} A_{n,m_0} A_{n,m_1} \cos(\psi_{P,n,m_0} - \psi_{P,n,m_1}) \quad (2.43)$$

$$\mathbb{E} [y_P(t)^4] = \frac{3}{8} \Re \left\{ \sum_{\substack{n_0, n_1, n_2, n_3 \\ n_0 + n_1 = n_2 + n_3}} \mathbf{h}_{n_0} \mathbf{w}_{P,n_0} \mathbf{h}_{n_1} \mathbf{w}_{P,n_1} (\mathbf{h}_{n_2} \mathbf{w}_{P,n_2})^* (\mathbf{h}_{n_3} \mathbf{w}_{P,n_3})^* \right\} \quad (2.44)$$

$$= \frac{3}{8} \sum_{\substack{n_0, n_1, n_2, n_3 \\ n_0 + n_1 = n_2 + n_3}} \sum_{m_0, m_1, m_2, m_3} \left[\prod_{j=0}^3 s_{P,n_j, m_j} A_{n_j, m_j} \right] \cos(\psi_{P,n_0, m_0} + \psi_{P,n_1, m_1} - \psi_{P,n_2, m_2} - \psi_{P,n_3, m_3}) \quad (2.45)$$

We then turn to the multicarrier modulated waveform $y_I(t)$. It can be treated as a multisine waveform for the input symbols $\{\tilde{x}_n\}$ that vary randomly with symbol rate $1/B_s$. Similarly, the approximated DC current provided by the rectifier is given by

$$i_{\text{out}} \approx k'_0 + \sum_{i \text{ even}, i \geq 2}^{n_o} k'_i \rho^{i/2} R_{\text{ant}}^{i/2} \mathbb{E}_{\{\tilde{x}_n\}} \left[y_I(t)^i \right] \quad (2.46)$$

To obtain the expectation, we first extract the DC currents corresponding to a given set of amplitudes $\{\tilde{s}_{I,n,m}\}$ and phases $\{\tilde{\phi}_{I,n,m}\}$, then take the expectation over the distribution of the input symbol \tilde{x}_n . As an i.i.d. CSCG distribution $\tilde{x}_n \sim \mathcal{CN}(0, 1)$ is assumed, the amplitude square $|\tilde{x}_n|^2$ is exponentially distributed with $\mathbb{E}[|\tilde{x}_n|^2] = 1$. Using the moment generating function, we also have $\mathbb{E}[|\tilde{x}_n|^4] = \mathbb{E}\left[(|\tilde{x}_n|^2)^2\right] = 2$. Note this gain applies to the output current, which measures the contribution of modulation and does not exist for multisine waveform. Following [11], we can obtain the expectation of the received information waveform to the second and fourth orders

$$\mathbb{E}[y_I(t)^2] = \frac{1}{2} \sum_{n=0}^{N-1} \sum_{m_0, m_1} s_{I,n,m_0} s_{I,n,m_1} A_{n,m_0} A_{n,m_1} \cos(\psi_{I,n,m_0} - \psi_{I,n,m_1}) \quad (2.47)$$

$$= \frac{1}{2} \sum_{n=0}^{N-1} |\mathbf{h}_n \mathbf{w}_{I,n}|^2 \quad (2.48)$$

$$\mathbb{E}[y_I(t)^4] = \frac{6}{8} \sum_{n_0, n_1} \sum_{m_0, m_1, m_2, m_3} \left[\prod_{j=0,2} s_{I,n_0,m_j} A_{n_0,m_j} \right] \left[\prod_{j=1,3} s_{I,n_1,m_j} A_{n_1,m_j} \right] \cos(\psi_{I,n_0,m_0} + \psi_{I,n_1,m_1} - \psi_{I,n_0,m_2} - \psi_{I,n_1,m_3}) \quad (2.49)$$

$$= \frac{6}{8} \left[\sum_{n=0}^{N-1} |\mathbf{h}_n \mathbf{w}_{I,n}|^2 \right]^2 \quad (2.50)$$

It is worth noting that the truncation order n_o in equation 2.46 determines the relationship between the received signal and the harvested power. On top of it, [10] proposed two diode models:

- *diode linear model* ($n_o = 2$) is the conventional perspective that assumes the total output power is the sum of the subband power. It omits the rectifier nonlinearity and is typically suitable for a very low input power (below -30 dBm).
- *diode nonlinear model* ($n_o > 2$) considers the contributions of higher order terms to the harvested power. It captures the nonlinear behavior of the diode with the product terms that consist of contributions from different frequencies (as indicated by n_0, n_1 in equation 2.49 and 2.44). The model is complicated but accurate, and especially fits the low power regime between -30 dBm and 0 dBm.

In the diode linear model corresponding to equations 2.42 and 2.47, the output current is only a function of $\sum_{n=0}^{N-1} |\mathbf{h}_n \mathbf{w}_{P/I,n}|^2$. Hence, it appears that multicarrier multisine and modulated waveforms are equally suitable for WPT. On the other hand, the diode nonlinear model highlights a clear difference between the power delivered by both waveforms. For the modulated component, the second and fourth order terms in 2.47 and 2.49 share same dependencies on $\sum_{n=0}^{N-1} |\mathbf{h}_n \mathbf{w}_{I,n}|^2$. It implies that for a modulated waveform with CSCG inputs, the higher order terms behave similarly to the second order term and both models are equivalent. In comparison, for the multisine waveform, the terms 2.42 and 2.44 are decomposed as the product of contributions from different subbands. Also, the second order term is linear as a sum over each frequencies while the nonlinear fourth order term shows some cross correlation between different subbands.

In this paper, we set $n_o = 4$ to explore the fundamental nonlinear behaviour of the diode and its impact on the harvested current. Since $\mathbb{E}[y_P(t)y_I(t)] = \mathbb{E}[y_P(t)^3 y_I(t)] = \mathbb{E}[y_P(t)y_I(t)^3] = 0$ and $\mathbb{E}[y_P(t)^2 y_I(t)^2] = \mathbb{E}[y_P(t)^2] \mathbb{E}[y_I(t)^2]$, the approximated output DC current of equation 2.15 reduces to

$$\begin{aligned} i_{\text{out}} \approx & k'_0 + k'_2 \rho R_{\text{ant}} \mathbb{E}[y_P(t)^2] + k'_4 \rho^2 R_{\text{ant}}^2 \mathbb{E}[y_P(t)^4] \\ & + k'_2 \rho R_{\text{ant}} \mathbb{E}[y_I(t)^2] + k'_4 \rho^2 R_{\text{ant}}^2 \mathbb{E}[y_I(t)^4] \\ & + 6k'_4 \rho^2 R_{\text{ant}}^2 \mathbb{E}[y_P(t)^2] \mathbb{E}[y_I(t)^2] \end{aligned} \quad (2.51)$$

whose corresponding target function is

$$\begin{aligned} z_{\text{DC}} \approx & k_0 + k_2 \rho R_{\text{ant}} \mathbb{E}[y_P(t)^2] + k_4 \rho^2 R_{\text{ant}}^2 \mathbb{E}[y_P(t)^4] \\ & + k_2 \rho R_{\text{ant}} \mathbb{E}[y_I(t)^2] + k_4 \rho^2 R_{\text{ant}}^2 \mathbb{E}[y_I(t)^4] \\ & + 6k_4 \rho^2 R_{\text{ant}}^2 \mathbb{E}[y_P(t)^2] \mathbb{E}[y_I(t)^2] \end{aligned} \quad (2.52)$$

Chapter 3

Rate-Energy Tradeoff

In this section, we first characterize the rate-energy region for the proposed system, then transform it into a general optimization problem. On top of it, we decouple the spatial and frequency design, investigate the lower bound of the superposed waveform, consider the PAPR constraint, and extend the GP method to MIMO cases.

3.1 Rate-Energy Region Characterization

The achievable rate-energy region is defined as

$$C_{R-I_{DC}}(P) \triangleq \left\{ (R, I_{DC}) : R \leq I, I_{DC} \leq i_{\text{out}}, \frac{1}{2} [\|\mathbf{S}_I\|_F^2 + \|\mathbf{S}_P\|_F^2] \leq P \right\} \quad (3.1)$$

where (R, I_{DC}) is the rate-energy pair, P is the transmit power budget, I is the mutual information, I_{DC} is the harvested DC current, i_{out} is the rectifier output current, and $\mathbf{S}_I, \mathbf{S}_P$ hold the amplitudes of information and power signals respectively. With the target function z_{DC} given by 2.52, it is redefined in [11] as

$$C_{R-I_{DC}}(P) \triangleq \left\{ (R, I_{DC}) : R \leq I, I_{DC} \leq z_{DC}, \frac{1}{2} [\|\mathbf{S}_I\|_F^2 + \|\mathbf{S}_P\|_F^2] \leq P \right\} \quad (3.2)$$

To obtain the maximum rate-energy region, we aim to find the optimal amplitudes $\mathbf{S}_I^*, \mathbf{S}_P^*$ and phases Φ_I^*, Φ_P^* for both waveforms at the transmitter, and obtain the best power splitting ratio ρ^* at the receiver. It is assumed in the optimization that perfect CSIT is available in the form of channel frequency response $h_{n,m}$.

3.2 Problem Formulation

For the MISO case, the optimal phase from rate and energy perspectives can be derived from the mutual information in 2.40, the target function in 2.52, and the waveform expressions in 2.42 – 2.50. The solutions correspond to the matched filters w.r.t. the phases of the channel

$$\phi_{I,n,m}^* = \phi_{P,n,m}^* = -\bar{\psi}_{n,m} \quad (3.3)$$

Such phase decisions can guarantee all the cosine terms in 2.42 – 2.50 are maximized by setting the arguments to 0. Φ_I^* and Φ_P^* can be constructed by collecting $\phi_{I,n,m}^*$ and $\phi_{P,n,m}^*$ to the (n, m) entries respectively. On top of that, the target function $z_{DC}(\mathbf{S}_P, \mathbf{S}_I, \Phi_P^*, \Phi_I^*, \rho)$ can be further written as

$$\begin{aligned}
z_{DC} = & \frac{k_2 \rho}{2} R_{\text{ant}} \sum_{n=0}^{N-1} \sum_{m_0, m_1} \left[\prod_{j=0}^1 s_{P,n,m_j} A_{n,m_j} \right] \\
& + \frac{3k_4 \rho^2}{8} R_{\text{ant}}^2 \sum_{\substack{n_0, n_1, n_2, n_3 \\ n_0 + n_1 = n_2 + n_3}} \sum_{m_0, m_1, m_2, m_3} \left[\prod_{j=0}^3 s_{P,n_j,m_j} A_{n_j,m_j} \right] \\
& + \frac{k_2 \rho}{2} R_{\text{ant}} \sum_{n=0}^{N-1} \sum_{m_0, m_1} \left[\prod_{j=0}^1 s_{I,n,m_j} A_{n,m_j} \right] \\
& + \frac{3k_4 \rho^2}{4} R_{\text{ant}}^2 \sum_{n_0, n_1} \sum_{m_0, m_1, m_2, m_3} \left[\prod_{j=0,2} s_{I,n_0,m_j} A_{n_0,m_j} \right] \left[\prod_{j=1,3} s_{I,n_1,m_j} A_{n_1,m_j} \right] \\
& + \frac{3k_4 \rho^2}{2} R_{\text{ant}}^2 \left[\sum_{n=0}^{N-1} \sum_{m_0, m_1} \left[\prod_{j=0}^1 s_{P,n,m_j} A_{n,m_j} \right] \right] \left[\sum_{n=0}^{N-1} \sum_{m_0, m_1} \left[\prod_{j=0}^1 s_{I,n,m_j} A_{n,m_j} \right] \right]
\end{aligned} \tag{3.4}$$

Also, [33] demonstrated that using matched filter for amplitude design leads to a performance close to the optimal one. Therefore, it can be employed as a feasible initialization for the optimization. On antenna m and subband n , the amplitudes of power and information waveform are initialized to

$$s_{P,n,m} = s_{I,n,m} = c A_{n,m} \tag{3.5}$$

where c is the constant to guarantee the transmit power constraint.

On the other hand, the mutual information is given by

$$I(\mathbf{S}_I, \Phi_I^*, \rho) = \log_2 \left(\prod_{n=0}^{N-1} \left(1 + \frac{(1-\rho)}{\sigma_n^2} C_n \right) \right) \tag{3.6}$$

where $C_n = \sum_{m_0, m_1} \prod_{j=0}^1 s_{I,n,m_j} A_{n,m_j}$.

Note both the target function and mutual information are posynomials [36]. Therefore, one possible approach to characterize the rate-energy region is to transform the optimization into an energy maximization problem with average transmit power budget P and rate constraint \bar{R}

$$\max_{\mathbf{S}_P, \mathbf{S}_I, \rho} z_{DC}(\mathbf{S}_P, \mathbf{S}_I, \Phi_P^*, \Phi_I^*, \rho) \tag{3.7}$$

$$\text{subject to } \frac{1}{2} [\|\mathbf{S}_I\|_F^2 + \|\mathbf{S}_P\|_F^2] \leq P, \tag{3.8}$$

$$I(\mathbf{S}_I, \Phi_I^*, \rho) \geq \bar{R} \tag{3.9}$$

Although the problem is not a standard Geometric Programming (GP), we can transform it to a Reversed GP by introducing an auxiliary variable t_0 [37]

$$\min_{\mathbf{S}_P, \mathbf{S}_I, \rho, t_0} 1/t_0 \quad (3.10)$$

$$\text{subject to} \quad \frac{1}{2} [\|\mathbf{S}_I\|_F^2 + \|\mathbf{S}_P\|_F^2] \leq P \quad (3.11)$$

$$t_0/z_{DC}(\mathbf{S}_P, \mathbf{S}_I, \Phi_P^*, \Phi_I^*, \rho) \leq 1 \quad (3.12)$$

$$2^{\bar{R}} / \left[\prod_{n=0}^{N-1} \left(1 + \frac{(1-\rho)}{\sigma_n^2} C_n \right) \right] \leq 1 \quad (3.13)$$

The new problem so far is not a standard GP as $1/z_{DC}(\mathbf{S}_P, \mathbf{S}_I, \Phi_P^*, \Phi_I^*, \rho)$ and $1/\left[\prod_{n=0}^{N-1} \left(1 + \frac{(1-\rho)}{\sigma_n^2} C_n \right)\right]$ are not posynomials. To solve this, [11] suggested a conservative approach to approximate the terms with posynomials in the denominator by new posynomials, based on the Arithmetic Mean-Geometric Mean (AM-GM) inequality.

Consider constraint 3.12 first. The posynomial at the denominator can be decomposed as sum of monomials

$$z_{DC}(\mathbf{S}_P, \mathbf{S}_I, \Phi_P^*, \Phi_I^*, \rho) = \sum_{k=1}^K g_k(\mathbf{S}_P, \mathbf{S}_I, \Phi_P^*, \Phi_I^*, \rho) \quad (3.14)$$

Since monomial $\{g_k\}$ is nonnegative for all k , the AM-GM inequality suggests a posynomial upper bound for the previous non-posynomial term

$$\frac{1}{\sum_{k=1}^K g_k(\mathbf{S}_P, \mathbf{S}_I, \Phi_P^*, \Phi_I^*, \rho)} \leq \prod_{k=1}^K \left(\frac{g_k(\mathbf{S}_P, \mathbf{S}_I, \Phi_P^*, \Phi_I^*, \rho)}{\gamma_k} \right)^{-\gamma_k} \quad (3.15)$$

The nonnegative coefficients $\{\gamma_k\}$ are chosen to satisfy $\sum_{k=1}^K \gamma_k = 1$. Similarly, define $\bar{\rho} = 1 - \rho$ and let $\{g_{nk}(\mathbf{S}_I, \bar{\rho})\}$ be the monomials of the posynomial $1 + \frac{\bar{\rho}}{\sigma_n^2} C_n$

$$1 + \frac{\bar{\rho}}{\sigma_n^2} C_n = \sum_{k=1}^{K_n} g_{nk}(\mathbf{S}_I, \bar{\rho}) \quad (3.16)$$

Apply the AM-GM inequality to 3.16, we have

$$\frac{1}{1 + \frac{\bar{\rho}}{\sigma_n^2} C_n} \leq \prod_{k=1}^{K_n} \left(\frac{g_{nk}(\mathbf{S}_I, \bar{\rho})}{\gamma_{nk}} \right)^{-\gamma_{nk}} \quad (3.17)$$

with $\gamma_{nk} \geq 0$ and $\sum_{k=1}^{K_n} \gamma_{nk} = 1$. In this way, we transformed the problem into a standard GP

$$\min_{\mathbf{S}_P, \mathbf{S}_I, \rho, \bar{\rho}, t_0} 1/t_0 \quad (3.18)$$

$$\text{subject to} \quad \frac{1}{2} [\|\mathbf{S}_I\|_F^2 + \|\mathbf{S}_P\|_F^2] \leq P \quad (3.19)$$

$$t_0 \prod_{k=1}^K \left(\frac{g_k(\mathbf{S}_P, \mathbf{S}_I, \Phi_P^*, \Phi_I^*, \rho)}{\gamma_k} \right)^{-\gamma_k} \leq 1 \quad (3.20)$$

$$2^{\bar{R}} \prod_{n=0}^{N-1} \prod_{k=1}^{K_n} \left(\frac{g_{nk}(\mathbf{S}_I, \bar{\rho})}{\gamma_{nk}} \right)^{-\gamma_{nk}} \leq 1 \quad (3.21)$$

$$\rho + \bar{\rho} \leq 1 \quad (3.22)$$

It is worth noting that the tightness of the AM-GM inequality depends on the choice of $\{\gamma_k, \gamma_{nk}\}$. In this paper, we employ the iterative method proposed in [11] that updates the coefficient sets at iteration i with the previous solution $\mathbf{S}_P^{(i-1)}, \mathbf{S}_I^{(i-1)}, \rho^{(i-1)}$

$$\gamma_k = \frac{g_k \left(\mathbf{S}_P^{(i-1)}, \mathbf{S}_I^{(i-1)}, \rho^{(i-1)} \right)}{z_{DC} \left(\mathbf{S}_P^{(i-1)}, \mathbf{S}_I^{(i-1)}, \rho^{(i-1)} \right)}, \quad k = 1, \dots, K \quad (3.23)$$

$$\gamma_{nk} = \frac{g_{nk} \left(\mathbf{S}_I^{(i-1)}, \bar{\rho}^{(i-1)} \right)}{1 + \frac{\bar{\rho}^{(i-1)}}{\sigma_n^2} C_n \left(\mathbf{S}_I^{(i-1)} \right)}, \quad n = 0, \dots, N-1, \quad k = 1, \dots, K_n \quad (3.24)$$

Once $\{\gamma_k, \gamma_{nk}\}$ are obtained, we solve problem 3.18 – 3.22 to obtain $\mathbf{S}_P^{(i)}, \mathbf{S}_I^{(i)}, \rho^{(i)}$. The iterations are repeated until convergence. Algorithm 1 summarizes all the procedures involved in the optimization. The successive approximation approach is also known as inner approximation method [38], which cannot guarantee a global optimal solution but the converged point satisfies the KKT conditions.

Algorithm 1 General Waveform Design

- 1: **Initialize:** $i \leftarrow 0$, Φ_P^*, Φ_I^* in 3.3, $\mathbf{S}_P, \mathbf{S}_I$ in 3.5, $\rho, \bar{\rho} = 1 - \rho$, $\bar{R}, z_{DC}^{(0)} = 0$
 - 2: **repeat**
 - 3: $i \leftarrow i + 1, \ddot{\mathbf{S}}_P \leftarrow \mathbf{S}_P, \ddot{\mathbf{S}}_I \leftarrow \mathbf{S}_I, \ddot{\rho} \leftarrow \rho, \ddot{\bar{\rho}} \leftarrow \bar{\rho}$
 - 4: $\gamma_k \leftarrow g_k \left(\ddot{\mathbf{S}}_P, \ddot{\mathbf{S}}_I, \Phi_P^*, \Phi_I^*, \ddot{\rho} \right) / z_{DC} \left(\ddot{\mathbf{S}}_P, \ddot{\mathbf{S}}_I, \Phi_P^*, \Phi_I^*, \ddot{\rho} \right), k = 1, \dots, K$
 - 5: $\gamma_{nk} \leftarrow g_{nk} \left(\ddot{\mathbf{S}}_I, \ddot{\rho} \right) / \left(1 + \frac{\ddot{\rho}}{\sigma_n^2} C_n \left(\ddot{\mathbf{S}}_I \right) \right), n = 0, \dots, N-1, k = 1, \dots, K_n$
 - 6: $\mathbf{S}_P, \mathbf{S}_I, \rho, \bar{\rho} \leftarrow \arg \min 3.18 - 3.22$
 - 7: $z_{DC}^{(i)} \leftarrow z_{DC} \left(\mathbf{S}_P, \mathbf{S}_I, \Phi_P^*, \Phi_I^*, \rho \right)$
 - 8: **until** $\left| z_{DC}^{(i)} - z_{DC}^{(i-1)} \right| < \text{or } i = i_{\max}$
-

3.3 Decoupled Design

For the transmitter with multiple antennas ($M > 1$), the previous method is involved with weight design across space and frequency. In this part, we will investigate an approach proposed in [11] that decouples the optimization in spatial and frequency domains without impacting performance. As suggested by equations 2.40 and 2.42 – 2.50, to maximize the rate and energy, the optimum weight vectors $\mathbf{w}_{P,n}$ and $\mathbf{w}_{I,n}$ correspond to the MRT beamformers

$$\begin{cases} \mathbf{w}_{P,n} = s_{P,n} \mathbf{h}_n^H / \|\mathbf{h}_n\| \\ \mathbf{w}_{I,n} = s_{I,n} \mathbf{h}_n^H / \|\mathbf{h}_n\| \end{cases} \quad (3.25)$$

Therefore, from equation 2.38, we have

$$\begin{cases} y_P(t) = \sum_{n=0}^{N-1} \|\mathbf{h}_n\|_{s_{P,n}} \cos(w_n t) = \Re \left\{ \sum_{n=0}^{N-1} \|\mathbf{h}_n\|_{s_{P,n}} e^{jw_n t} \right\} \\ y_I(t) = \sum_{n=0}^{N-1} \|\mathbf{h}_n\|_{s_{I,n} \tilde{x}_n} \cos(w_n t) = \Re \left\{ \sum_{n=0}^{N-1} \|\mathbf{h}_n\|_{s_{I,n} \tilde{x}_n} e^{jw_n t} \right\} \end{cases} \quad (3.26)$$

In this way, the weight optimization on multiple transmit antennas is converted into an equivalent problem on a single antenna. For the n -th subband, the equivalent channel gain is $\|\mathbf{h}_n\|$ with power $s_{P,n}^2$ and $s_{I,n}^2$ allocated to multisine and modulated waveform respectively (with power budget $\frac{1}{2} \sum_{n=0}^{N-1} (s_{P,n}^2 + s_{I,n}^2) = P$). The problem can be solved with Algorithm 1, with the second and fourth order terms reduce to

$$\begin{aligned} \mathbb{E}[y_P(t)^2] &= \frac{1}{2} \sum_{n=0}^{N-1} \|\mathbf{h}_n\|^2 s_{P,n}^2 \\ \mathbb{E}[y_P(t)^4] &= \frac{3}{8} \sum_{\substack{n_0, n_1, n_2, n_3 \\ n_0 + n_1 = n_2 + n_3}} \left[\prod_{j=0}^3 s_{P, n_j} \|\mathbf{h}_{n_j}\| \right] \\ \mathbb{E}[y_I(t)^2] &= \frac{1}{2} \sum_{n=0}^{N-1} \|\mathbf{h}_n\|^2 s_{I,n}^2 \\ \mathbb{E}[y_I(t)^4] &= \frac{6}{8} \left[\sum_{n=0}^{N-1} \|\mathbf{h}_n\|^2 s_{I,n}^2 \right]^2 \end{aligned} \quad (3.27)$$

Hence, the target function z_{DC} is only a function of two N -dimensional vectors $\mathbf{s}_{P/I} = [s_{P/I,0}, \dots, s_{P/I,N-1}]$, and the mutual information can be simplified as

$$I(\mathbf{s}_I, \rho) = \log_2 \left(\prod_{n=0}^{N-1} \left(1 + \frac{(1-\rho)}{\sigma_n^2} s_{I,n}^2 \|\mathbf{h}_n\|^2 \right) \right) \quad (3.28)$$

Similarly, we decompose the posynomials $z_{DC}(\mathbf{s}_P, \mathbf{s}_I, \rho) = \sum_{k=1}^K g_k(\mathbf{s}_P, \mathbf{s}_I, \rho)$ and $1 + \frac{\bar{\rho}}{\sigma_n^2} C_n = \sum_{k=1}^{K_n} g_{nk}(\mathbf{s}_I, \bar{\rho})$ with $C_n = s_{I,n}^2 \|\mathbf{h}_n\|^2$, then apply the AM-GM inequality to the constraints with posynomials in the denominator. The equivalent GP problem write as

$$\min_{\mathbf{s}_P, \mathbf{s}_I, \rho, \bar{\rho}, t_0} \quad 1/t_0 \quad (3.29)$$

$$\text{subject to} \quad \frac{1}{2} [\|\mathbf{s}_I\|^2 + \|\mathbf{s}_P\|^2] \leq P \quad (3.30)$$

$$t_0 \prod_{k=1}^K \left(\frac{g_k(\mathbf{s}_P, \mathbf{s}_I, \rho)}{\gamma_k} \right)^{-\gamma_k} \leq 1 \quad (3.31)$$

$$2^{\bar{R}} \prod_{n=0}^{N-1} \prod_{k=1}^{K_n} \left(\frac{g_{nk}(\mathbf{s}_I, \bar{\rho})}{\gamma_{nk}} \right)^{-\gamma_{nk}} \leq 1 \quad (3.32)$$

$$\rho + \bar{\rho} \leq 1 \quad (3.33)$$

Similar to 3.5, the amplitudes of power and information waveform can be initialized to

$$s_{P,n} = s_{I,n} = c \|\mathbf{h}_n\| \quad (3.34)$$

Compared with the general approach, the decoupled design guarantees the same performance by a joint space-frequency design with a lower computational complexity, which converts the original $N \times M$ matrices $\mathbf{S}_P, \mathbf{S}_I$ to N -dimensional vectors $\mathbf{s}_P, \mathbf{s}_I$ via MRT beamformers. Algorithm summarizes the optimization process for the decoupling strategy.

Algorithm 2 Decoupled Waveform Design

- 1: **Initialize:** $i \leftarrow 0$, Φ_P^*, Φ_I^* in 3.3, $\mathbf{s}_P, \mathbf{s}_I$ in 3.34, $\rho, \bar{\rho} = 1 - \rho$, $\bar{R}, z_{DC}^{(0)} = 0$
 - 2: **repeat**
 - 3: $i \leftarrow i + 1, \ddot{\mathbf{s}}_P \leftarrow \mathbf{s}_P, \ddot{\mathbf{s}}_I \leftarrow \mathbf{s}_I, \ddot{\rho} \leftarrow \rho, \ddot{\bar{\rho}} \leftarrow \bar{\rho}$
 - 4: $\gamma_k \leftarrow g_k(\ddot{\mathbf{s}}_P, \ddot{\mathbf{s}}_I, \Phi_P^*, \Phi_I^*, \ddot{\rho}) / z_{DC}(\ddot{\mathbf{s}}_P, \ddot{\mathbf{s}}_I, \Phi_P^*, \Phi_I^*, \ddot{\rho}), k = 1, \dots, K$
 - 5: $\gamma_{nk} \leftarrow g_{nk}(\ddot{\mathbf{s}}_I, \ddot{\rho}) / \left(1 + \frac{\ddot{\rho}}{\sigma_n^2} C_n(\ddot{\mathbf{s}}_I)\right), n = 0, \dots, N-1, k = 1, \dots, K_n$
 - 6: $\mathbf{s}_P, \mathbf{s}_I, \rho, \bar{\rho} \leftarrow \arg \min 3.29 - 3.33$
 - 7: $z_{DC}^{(i)} \leftarrow z_{DC}(\mathbf{s}_P, \mathbf{s}_I, \Phi_P^*, \Phi_I^*, \rho)$
 - 8: **until** $|z_{DC}^{(i)} - z_{DC}^{(i-1)}| < \epsilon$ or $i = i_{\max}$
-

3.4 Twofold Benefit of Superposed Waveform

The deterministic multisine waveform not only boosts the harvested energy but also avoids interference to the modulated waveform. To highlight its contribution to the twofold benefit, we compare the performance of superposed waveform to two baselines. In the first one, there is no multisine component and only modulated waveform is used for WIPT (i.e. $\mathbf{S}_P = 0, \frac{1}{2} \|\mathbf{S}_I\|_F^2 = P$). Therefore, the twofold benefit disappears. In contrast, it is assumed for the second baseline that the power waveform behaves as a deterministic multisine for energy delivery but as CSCG distributed for information transmission. In this configuration, the energy benefit of the multisine is maintained but the rate benefit is lost, as the power waveform creates an interference term $\sqrt{1 - \bar{\rho}} \mathbf{h}_n \mathbf{w}_{P,n}$. The achievable rate for this configuration writes as

$$I_{LB}(\mathbf{S}_P, \mathbf{S}_I, \Phi_P, \Phi_I, \rho) = \sum_{n=0}^{N-1} \log_2 \left(1 + \frac{(1 - \rho) |\mathbf{h}_n \mathbf{w}_{I,n}|^2}{\sigma_n^2 + (1 - \rho) |\mathbf{h}_n \mathbf{w}_{P,n}|^2} \right) \quad (3.35)$$

It contributes to a smaller rate-energy region compared with the one produced by the superposed waveform. It is important to notice that the MRT beamformers in 3.25 is not optimal due to the interference term. Also, the phases Φ_P^* and Φ_I^* by 3.3 are not best solutions for $M > 1$. The problem requires a more general approach for the joint weight design over space and frequency domains.

Consider the suboptimal phases Φ_P^* and Φ_I^* in 3.3 for simplicity. In such cases, the target function is given by equation 2.52 and the lower bound on the achievable rate can be expressed as

$$I_{LB}(\mathbf{S}_I, \Phi_I^*, \rho) = \log_2 \left(\prod_{n=0}^{N-1} \left(1 + \frac{(1-\rho)C_n}{\sigma_n^2 + (1-\rho)D_n} \right) \right) \quad (3.36)$$

with $C_n = \sum_{m_0, m_1} \prod_{j=0}^1 s_{I,n,m_j} A_{n,m_j}$ and $D_n = \sum_{m_0, m_1} \prod_{j=0}^1 s_{P,n,m_j} A_{n,m_j}$. Therefore, the problem is formulated into 3.10 – 3.13 with 3.13 replaced by

$$2^{\bar{R}} \frac{\prod_{n=0}^{N-1} \left(1 + \frac{\bar{\rho}}{\sigma_n^2} D_n \right)}{\prod_{n=0}^{N-1} \left(1 + \frac{\bar{\rho}}{\sigma_n^2} (D_n + C_n) \right)} \leq 1 \quad (3.37)$$

Decompose the posynomials in the denominators as

$$1 + \frac{\bar{\rho}}{\sigma_n^2} (D_n + C_n) = \sum_{j=1}^{J_n} f_{nj}(\mathbf{S}_P, \mathbf{S}_I, \rho) \quad (3.38)$$

where $\{f_{nj}(\mathbf{S}_P, \mathbf{S}_I, \rho)\}$ is the monomial terms. With a proper choice of nonnegative $\{\gamma_{nj}\}$ such that $\sum_{j=1}^{J_n} \gamma_{nj} = 1$, the standard GP can be written as

$$\min_{\mathbf{S}_P, \mathbf{S}_I, \rho, \bar{\rho}, t_0} \quad 1/t_0 \quad (3.39)$$

$$\text{subject to} \quad \frac{1}{2} [\|\mathbf{S}_I\|_F^2 + \|\mathbf{S}_P\|_F^2] \leq P \quad (3.40)$$

$$t_0 \prod_{k=1}^K \left(\frac{g_k(\mathbf{S}_P, \mathbf{S}_I, \Phi_P^*, \Phi_I^*, \rho)}{\gamma_k} \right)^{-\gamma_k} \leq 1 \quad (3.41)$$

$$2^{\bar{R}} \prod_{n=0}^{N-1} \left(1 + \frac{\bar{\rho}}{\sigma_n^2} D_n(\mathbf{S}_P) \right) \prod_{j=1}^{J_n} \left(\frac{f_{nj}(\mathbf{S}_P, \mathbf{S}_I, \rho)}{\gamma_{nj}} \right)^{-\gamma_{nj}} \leq 1 \quad (3.42)$$

$$\rho + \bar{\rho} \leq 1 \quad (3.43)$$

Algorithm shows the basic idea to obtain the lower-bound of rate-energy region. It boils down to Algorithm 1 when the interference posynomial $D_n = 0$ for all n .

Algorithm 3 Lower-Bound of R-E Region

- 1: **Initialize:** $i \leftarrow 0$, $\mathbf{w}_{P,n}, \mathbf{w}_{I,n}$ in 3.25, $\mathbf{S}_P, \mathbf{S}_I$ in 3.5, $\rho, \bar{\rho} = 1 - \rho$, $\bar{R}, z_{DC}^{(0)} = 0$
 - 2: **repeat**
 - 3: $i \leftarrow i + 1$, $\ddot{\mathbf{S}}_P \leftarrow \mathbf{S}_P, \ddot{\mathbf{S}}_I \leftarrow \mathbf{S}_I, \ddot{\rho} \leftarrow \rho, \ddot{\bar{\rho}} \leftarrow \bar{\rho}$
 - 4: $\gamma_k \leftarrow g_k(\ddot{\mathbf{S}}_P, \ddot{\mathbf{S}}_I, \ddot{\rho}) / z_{DC}(\ddot{\mathbf{S}}_P, \ddot{\mathbf{S}}_I, \ddot{\rho})$, $k = 1, \dots, K$
 - 5: $\gamma_{nj} \leftarrow f_{nj}(\ddot{\mathbf{S}}_P, \ddot{\mathbf{S}}_I, \ddot{\rho}) / \left(1 + \frac{\ddot{\rho}}{\sigma_n^2} (D_n(\ddot{\mathbf{S}}_P) + C_n(\ddot{\mathbf{S}}_I)) \right)$
 - 6: $\mathbf{S}_P, \mathbf{S}_I, \rho, \bar{\rho} \leftarrow \arg \min 3.39 - 3.43$
 - 7: $z_{DC}^{(i)} \leftarrow z_{DC}(\mathbf{S}_P, \mathbf{S}_I, \rho)$
 - 8: **until** $|z_{DC}^{(i)} - z_{DC}^{(i-1)}| < \epsilon$ or $i = i_{\max}$
-

3.5 PAPR Constraints

Another practical constraint for the transmitter is PAPR. As illustrated by figure 2.2(b), the modulated information waveform is a single sine with unit PAPR. Hence, the limitation on PAPR only influence the design of multisine power waveform. Following 2.30, the PAPR constraint on antenna m writes as

$$PAPR_m = \frac{\max_t |x_{P,m}(t)|^2}{\mathbb{E}[|x_{P,m}(t)|^2]} = \frac{\max_t |x_{P,m}(t)|^2}{\frac{1}{2}\|\mathbf{s}_{P,m}\|^2} \leq \eta \quad (3.44)$$

Assume the optimum phases Φ_P^*, Φ_I^* in equation 3.3 are used in the optimization of $\mathbf{S}_I, \mathbf{S}_P$. To transform inequation 3.44 into a solvable one, we introduce an oversampling factor O_s to obtain the discrete version of the multisine signal at $t_q = qT/NO_s$ for $q = 0, \dots, NO_s - 1$ with $T = 1/\Delta f$. For a sufficiently large O_s , the PAPR constraint can be expressed as

$$|x_{P,m}(t_q)|^2 \leq \frac{1}{2}\eta\|\mathbf{s}_{P,m}\|^2 \quad (3.45)$$

where the l.h.s. can be deducted from equation 2.30 as

$$|x_{P,m}(t_q)|^2 = \sum_{n_0, n_1} s_{P,n_0,m} s_{P,n_1,m} \cos(w_{n_0} t_q + \phi_{P,n_0,m}^*) \cos(w_{n_1} t_q + \phi_{P,n_1,m}^*) \quad (3.46)$$

However, $|x_{P,m}(t_q)|^2$ is no longer a posynomial because the time-varying arguments of the cosines produce some negative coefficients. Instead, it is actually a signomial which can be decomposed either as the sum of monomials with positive and negative coefficients, or as the difference of two posynomials

$$|x_{P,m}(t_q)|^2 = f_{mq}(\mathbf{S}_P, \Phi_P^*) = f_{mq1}(\mathbf{S}_P, \Phi_P^*) - f_{mq2}(\mathbf{S}_P, \Phi_P^*) \quad (3.47)$$

Therefore, the PAPR constraint rewrites as

$$\frac{f_{mq1}(\mathbf{S}_P, \Phi_P^*)}{\frac{1}{2}\eta\|\mathbf{s}_{P,m}\|^2 + f_{mq2}(\mathbf{S}_P, \Phi_P^*)} \leq 1 \quad (3.48)$$

Similarly, denote the posynomial at the denominator as

$$\frac{1}{2}\eta\|\mathbf{s}_{P,m}\|^2 + f_{mq2}(\mathbf{S}_P, \Phi_P^*) = \sum_{k=1}^{K_{mq2}} g_{mq2k}(\mathbf{S}_P, \Phi_P^*) \quad (3.49)$$

By a proper choice of nonnegative $\{\gamma_{mq2k}\}$ with $\sum_{k=1}^{K_{mq2}} \gamma_{mq2k} = 1$, we apply AM-GM inequality to 3.48 and obtain an equivalent inequation

$$f_{mq1}(\mathbf{S}_P, \Phi_P^*) \prod_{k=1}^{K_{mq2}} \left(\frac{g_{mq2k}(\mathbf{S}_P, \Phi_P^*)}{\gamma_{mq2k}} \right)^{-\gamma_{mq2k}} \leq 1 \quad (3.50)$$

In this way, the optimization problem 3.18 – 3.22 with an extra PAPR constraint 3.44 is replaced by a standard GP

$$\min_{\mathbf{S}_P, \mathbf{S}_I, \rho, \bar{\rho}, t_0} 1/t_0 \quad (3.51)$$

$$\text{subject to} \quad \frac{1}{2} [\|\mathbf{S}_I\|_F^2 + \|\mathbf{S}_P\|_F^2] \leq P \quad (3.52)$$

$$t_0 \prod_{k=1}^K \left(\frac{g_k(\mathbf{S}_P, \mathbf{S}_I, \Phi_P^*, \Phi_I^*, \rho)}{\gamma_k} \right)^{-\gamma_k} \leq 1 \quad (3.53)$$

$$2^{\bar{R}} \prod_{n=0}^{N-1} \prod_{k=1}^{K_n} \left(\frac{g_{nk}(\mathbf{S}_I, \bar{\rho})}{\gamma_{nk}} \right)^{-\gamma_{nk}} \leq 1 \quad (3.54)$$

$$f_{mq1}(\mathbf{S}_P, \Phi_P^*) \prod_{k=1}^{K_{mq2}} \left(\frac{g_{mq2k}(\mathbf{S}_P, \Phi_P^*)}{\gamma_{mq2k}} \right)^{-\gamma_{mq2k}} \leq 1 \quad (3.55)$$

$$\rho + \bar{\rho} \leq 1 \quad (3.56)$$

Algorithm 4 shows the gist of the optimization procedure. For the system with multiple transmit antenna and valid PAPR constraints, the decoupling strategy is suboptimal since the argument of cosines are indeed frequency-dependent. Also, the multisine waveform is oversampled to satisfy the PAPR constraint, which further increases the overall computational complexity.

Algorithm 4 Waveform Design with PAPR Constraints

- 1: **Initialize:** $i \leftarrow 0$, Φ_P^*, Φ_I^* in 3.3, $\mathbf{S}_P, \mathbf{S}_I$ in 3.5, $\rho, \bar{\rho} = 1 - \rho$, $\bar{R}, z_{DC}^{(0)} = 0$
 - 2: **repeat**
 - 3: $i \leftarrow i + 1$, $\ddot{\mathbf{S}}_P \leftarrow \mathbf{S}_P$, $\ddot{\mathbf{S}}_I \leftarrow \mathbf{S}_I$, $\ddot{\rho} \leftarrow \rho$, $\ddot{\bar{\rho}} \leftarrow \bar{\rho}$
 - 4: $\gamma_k \leftarrow g_k(\ddot{\mathbf{S}}_P, \ddot{\mathbf{S}}_I, \Phi_P^*, \Phi_I^*, \ddot{\rho}) / z_{DC}(\ddot{\mathbf{S}}_P, \ddot{\mathbf{S}}_I, \Phi_P^*, \Phi_I^*, \ddot{\rho})$, $k = 1, \dots, K$
 - 5: $\gamma_{nk} \leftarrow g_{nk}(\ddot{\mathbf{S}}_I, \ddot{\rho}) / \left(1 + \frac{\ddot{\rho}}{\sigma_n^2} C_n(\ddot{\mathbf{S}}_I)\right)$, $n = 0, \dots, N-1$, $k = 1, \dots, K_n$
 - 6: $\gamma_{mq2k} \leftarrow g_{mq2k}(\mathbf{S}_P, \Phi_P^*) / \left(\frac{1}{2}\eta \|\mathbf{S}_{P,m}\|^2 + f_{mq2}(\mathbf{S}_P, \Phi_P^*)\right)$, $m = 1, \dots, M$, $q = 0, \dots, NO_s - 1$, $k = 1, \dots, K_{mq2}$
 - 7: $\mathbf{S}_P, \mathbf{S}_I, \rho, \bar{\rho} \leftarrow \arg \min 3.51 - 3.56$
 - 8: $z_{DC}^{(i)} \leftarrow z_{DC}(\mathbf{S}_P, \mathbf{S}_I, \Phi_P^*, \Phi_I^*, \rho)$
 - 9: **until** $|z_{DC}^{(i)} - z_{DC}^{(i-1)}| < \epsilon$ or $i = i_{\max}$
-

3.6 Multiple Rectennas

The rate-energy region is expected to be enlarged with multiple rectennas. In this part, we extend the general MISO strategy in section 3.2 to U rectennas, which can either serve a single user in a point-to-point MIMO WIPT or spread across multiple users in a MU-MISO WIPT. Since the rectennas have specific preference on the transmitted waveform, there exists a tradeoff between the energy collected in different harvesters. The fairness issue can be solved by introducing weight v_u for rectenna $u = 1, \dots, U$ and considering the weighted sum of DC components as new target function

$$Z_{DC}(\mathbf{S}_P, \mathbf{S}_I, \Phi_P^*, \Phi_I^*, \rho) = \sum_{u=1}^U v_u z_{DC,u}(\mathbf{S}_P, \mathbf{S}_I, \Phi_P^*, \Phi_I^*, \rho) \quad (3.57)$$

With multiple rectennas, the frequency response is extended from 2.34 as

$$h_{n,m,u} = A_{n,m,u} e^{j\bar{\psi}_{n,m,u}} \quad (3.58)$$

Therefore, the phase of the received signal on rectenna u in subband n transmitted by antenna m is

$$\psi_{n,m,u} = \phi_{n,m} + \bar{\psi}_{n,m,u} \quad (3.59)$$

where $\phi_{n,m}$ is the beamforming phase. It is impossible to ensure $\psi_{n,m,u} = 0$ for all rectennas with three constraints n, m, u but only two variables n, m . Therefore, the arguments of cosines in 2.42 – 2.50 are not guaranteed as zero with a specific phase design Φ'_P, Φ'_I , and the target function $Z_{DC}(\mathbf{S}_P, \mathbf{S}_I, \Phi_P^*, \Phi_I^*, \rho)$ is indeed a signomial as some coefficients are negative.

For subband n , the channel matrix can be constructed as

$$\tilde{\mathbf{H}}_n = [\tilde{\mathbf{h}}_{n,1}^T \dots \tilde{\mathbf{h}}_{n,U}^T]^T \quad (3.60)$$

with $\tilde{\mathbf{h}}_{n,u} = \sqrt{k_2 v_u} \mathbf{h}_{n,u}$. It is argued in [10] that a possible choice of Φ'_P, Φ'_I is to set the (n, m) entries as $\phi'_{P,n,m} = \phi'_{I,n,m} = \angle v_{\max,n,m}$ where $v_{\max,n,m}$ is the m -th term of the dominant right singular vector $\mathbf{v}_{\max,n}$ that can be obtained through singular value decomposition of $\tilde{\mathbf{H}}_n$.

To convert the problem into a standard GP, we introduce an auxiliary variable t_0 and rewrite the signomial as the difference of two posynomials

$$Z_{DC}(\mathbf{S}_P, \mathbf{S}_I, \Phi'_P, \Phi'_I, \rho) = f_1(\mathbf{S}_P, \mathbf{S}_I, \Phi'_P, \Phi'_I, \rho) - f_2(\mathbf{S}_P, \mathbf{S}_I, \Phi'_P, \Phi'_I, \rho) \geq t_0 \quad (3.61)$$

Furthermore, decompose the first posynomial as

$$f_1(\mathbf{S}_P, \mathbf{S}_I, \Phi'_P, \Phi'_I, \rho) = \sum_{k=1}^{K_1} g_{1k}(\mathbf{S}_P, \mathbf{S}_I, \Phi'_P, \Phi'_I, \rho) \quad (3.62)$$

With a proper choice of nonnegative $\{\gamma_{1k}\}$ satisfying $\sum_{k=1}^{K_1} \gamma_{1k} = 1$, inequation 3.61 rewrites as

$$\frac{t_0 + f_2(\mathbf{S}_P, \mathbf{S}_I, \Phi'_P, \Phi'_I, \rho)}{f_1(\mathbf{S}_P, \mathbf{S}_I, \Phi'_P, \Phi'_I, \rho)} = (t_0 + f_2(\mathbf{S}_P, \mathbf{S}_I, \Phi'_P, \Phi'_I, \rho)) \prod_{k=1}^{K_1} \left(\frac{g_{1k}(\mathbf{S}_P, \mathbf{S}_I, \Phi'_P, \Phi'_I, \rho)}{\gamma_{1k}} \right)^{-\gamma_{1k}} \leq 1 \quad (3.63)$$

Similarly, the denominator of rate constraint 3.13 is indeed a product of signomials

$$1 + \frac{(1 - \rho)}{\sigma_n^2} C_n = f_{1nk}(\mathbf{S}_P, \mathbf{S}_I, \Phi'_P, \Phi'_I, \rho) - f_{2nk}(\mathbf{S}_P, \mathbf{S}_I, \Phi'_P, \Phi'_I, \rho) \quad (3.64)$$

Therefore, we can rewrite 3.13 as

$$\prod_{n=0}^{N-1} \left(1 + \frac{(1-\rho)}{\sigma_n^2} C_n \right) = \prod_{n=0}^{N-1} (f_{1nk}(\mathbf{S}_P, \mathbf{S}_I, \boldsymbol{\Phi}'_P, \boldsymbol{\Phi}'_I, \rho) - f_{2nk}(\mathbf{S}_P, \mathbf{S}_I, \boldsymbol{\Phi}'_P, \boldsymbol{\Phi}'_I, \rho)) \geq 2^{\bar{R}} \quad (3.65)$$

One possible approach is to unwrap the result of signomial multiplication as a new signomial. That is

$$f'_1(\mathbf{S}_P, \mathbf{S}_I, \boldsymbol{\Phi}'_P, \boldsymbol{\Phi}'_I, \rho) - f'_2(\mathbf{S}_P, \mathbf{S}_I, \boldsymbol{\Phi}'_P, \boldsymbol{\Phi}'_I, \rho) \geq 2^{\bar{R}} \quad (3.66)$$

which is equivalent to

$$\frac{2^{\bar{R}} + f'_2(\mathbf{S}_P, \mathbf{S}_I, \boldsymbol{\Phi}'_P, \boldsymbol{\Phi}'_I, \rho)}{f'_1(\mathbf{S}_P, \mathbf{S}_I, \boldsymbol{\Phi}'_P, \boldsymbol{\Phi}'_I, \rho)} \leq 1 \quad (3.67)$$

By decomposing $f'_1(\mathbf{S}_P, \mathbf{S}_I, \boldsymbol{\Phi}'_P, \boldsymbol{\Phi}'_I, \rho) = \sum_{k=1}^{K'_1} g'_{1k}(\mathbf{S}_P, \mathbf{S}_I, \boldsymbol{\Phi}'_P, \boldsymbol{\Phi}'_I, \rho)$ and introducing another nonnegative coefficient set $\{\gamma'_{1k}\}$ with $\sum_{k=1}^{K'_1} \gamma'_{1k} = 1$ for AM-GM inequality, it can be converted into constraint in standard form

$$2^{\bar{R}} + f'_2(\mathbf{S}_P, \mathbf{S}_I, \boldsymbol{\Phi}'_P, \boldsymbol{\Phi}'_I, \rho) \prod_{k=1}^{K'_1} \left(\frac{g'_{1k}(\mathbf{S}_P, \mathbf{S}_I, \boldsymbol{\Phi}'_P, \boldsymbol{\Phi}'_I, \rho)}{\gamma'_{1k}} \right)^{-\gamma'_{1k}} \leq 1 \quad (3.68)$$

Hence, the problem is transformed into a standard GP

$$\min_{\mathbf{S}_P, \mathbf{S}_I, \rho, \bar{\rho}, t_0} \quad 1/t_0 \quad (3.69)$$

$$\text{subject to} \quad \frac{1}{2} [\|\mathbf{S}_I\|_F^2 + \|\mathbf{S}_P\|_F^2] \leq P \quad (3.70)$$

$$(t_0 + f_2(\mathbf{S}_P, \mathbf{S}_I, \boldsymbol{\Phi}'_P, \boldsymbol{\Phi}'_I, \rho)) \prod_{k=1}^{K_1} \left(\frac{g_{1k}(\mathbf{S}_P, \mathbf{S}_I, \boldsymbol{\Phi}'_P, \boldsymbol{\Phi}'_I, \rho)}{\gamma_{1k}} \right)^{-\gamma_{1k}} \leq 1 \quad (3.71)$$

$$(2^{\bar{R}} + f'_2(\mathbf{S}_P, \mathbf{S}_I, \boldsymbol{\Phi}'_P, \boldsymbol{\Phi}'_I, \rho)) \prod_{k=1}^{K'_1} \left(\frac{g'_{1k}(\mathbf{S}_P, \mathbf{S}_I, \boldsymbol{\Phi}'_P, \boldsymbol{\Phi}'_I, \rho)}{\gamma'_{1k}} \right)^{-\gamma'_{1k}} \leq 1 \quad (3.72)$$

$$\rho + \bar{\rho} \leq 1 \quad (3.73)$$

It is worth noting that the GP method is not the best approach for waveform design, as the beamforming phases $\boldsymbol{\Phi}'_P, \boldsymbol{\Phi}'_I$ determined before optimization are sub-optimal. Another disadvantage of the proposed strategy is the unwrap process from 3.65 to 3.66 significantly increases the computational complexity and is typically suitable for small n and m .

Chapter 4

Performance Evaluation

In this section, we evaluate the performance of superposed waveform by applying the proposed algorithms to diode nonlinear model. A WiFi-like open space environment with multipath channel is assumed and simulated with HiperLAN/2 model B [39], where the 18 taps are modelled as i.i.d. CSCG variables with normalized total average power. Table 4.1 summarizes the reference parameters in the simulation. In the following sections, the settings will be employed unless otherwise stated.

Table 4.1: Reference parameters used in the simulation

	Parameter	Value
Transceiver	Truncation order	$n_o = 4$
	Diode k-parameters	$k_2 = 0.0034; k_4 = 0.3829$
	Antenna resistance	$R_{\text{ant}} = 50 \Omega$
	Transmit antenna	$M = 1$
	Receive antenna	$U = 1$
	Average transmit power	$P_{\text{rf}}^t = -20 \text{ dBm}$
	Average receive power	$P_{\text{rf}}^r = -20 \text{ dBm}$
	Average Noise power	$\sigma_n^2 = -40 \text{ dBm}$
	Effective isotropic radiated power	EIRP = 36 dBm
	Receive antenna gain	$G_r = 2 \text{ dBi}$
Channel	Minimum current gain per iteration	$\varepsilon = 0.05 \mu\text{A}$
	Center frequency	$f_0 = 5.18 \text{ GHz}$
	Path loss	$PL = 58 \text{ dB}$
	Tap	$L = 18$
	Bandwidth	$B = 1 \text{ MHz}$
	Subband	$N = 16$
	Frequency gap	$\Delta f = 62.5 \text{ kHz}$
	SNR	SNR = 20 dB

4.1 SISO

Figure 4.1 shows the frequency response of one realization of multipath FF and FS channel based on the same tap delays and gains.

In the R-E region, the rightmost point of each curve indicates the maximum achievable rate with zero harvested DC current. It corresponds to WIT where all

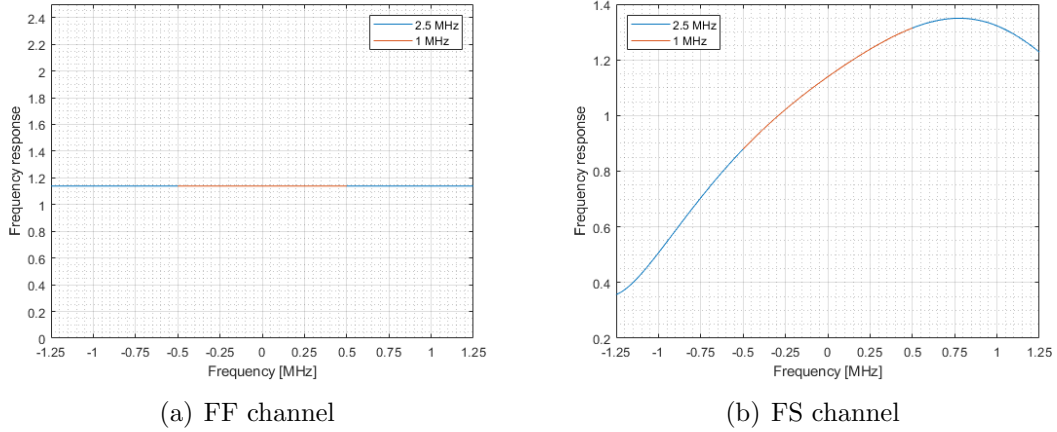


Figure 4.1: Frequency response of the SISO FF and FS channels

transmit power is allocated to the modulated information waveform by water-filling algorithm with $\rho = 0$. Note that the x-axis here refers to per-subband rate which is normalized w.r.t. bandwidth. Since the power budget is fixed, each subband indeed receives less power as N increases. Therefore, the total capacity increases but the rate achieved by each subband indeed decreases. On the other hand, the leftmost point corresponds to the maximum output DC current with zero information rate, which is realized by allocating all power to the multisine waveform with $\rho = 0$ (WPT).

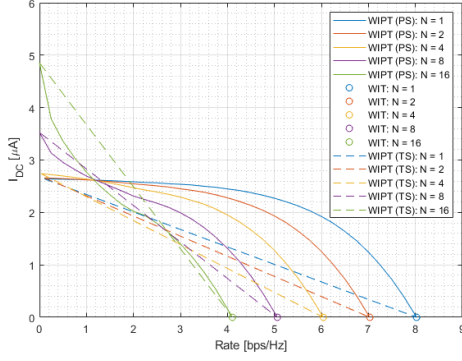
Nevertheless, the discrete rate constraint in WIPT optimization problem 3.7 – 3.9 prevents the solutions from achieving the absolute WIT points. Therefore, we performed individual WIT and combine the results to obtain the R-E plots. Also, the rate achieved by a certain solution can be slightly larger than the requirement, as the current gain of another iteration can be negligible (smaller than ε).

4.1.1 R-E Region vs Subband

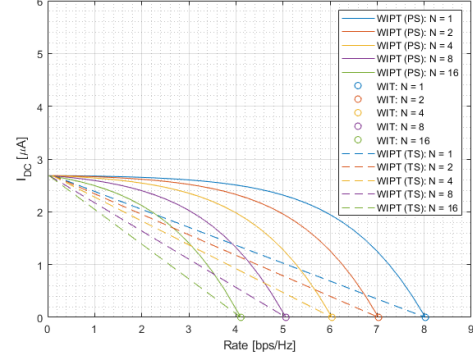
Figure 4.2 illustrates the R-E region against subband $N = 1, 2, 4, 8, 16$ for superposed waveform and no power waveform in FF and FS channels respectively.

It can be observed that the introduction of multisine power waveform boosts the harvested signal for $N > 4$ where the superposed waveform outperforms the modulated signal for WIPT. In contrast, the R-E performance of both signals are very close for $N \leq 4$ and the modulated waveform is preferred with lower complexity. The reason is that the fourth order terms of power and information waveforms 2.44 and 2.49 have different contribution to the harvested DC current. Despite both posynomials consist of monomials of similar magnitude ($\prod_{j=0}^3 s_{P,n_j,m_j} A_{n_j,m_j}$ and $\prod_{j=0,2} s_{I,n_0,m_j} A_{n_0,m_j} \prod_{j=1,3} s_{I,n_1,m_j} A_{n_1,m_j}$), the power posynomial contains $(2N^3 + N)/3$ monomials but the information posynomial only holds N^2 monomials. Therefore, the benefit of multisine power waveform on the harvested power is amplified with a large N . Although it seems that a very large N can further increases the output DC current, this is not the case as each subband receives less portion and the amplitude of monomials decreases accordingly.

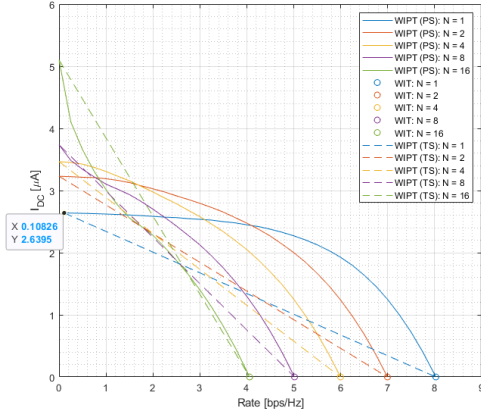
A contrast of R-E plots on FF and FS channels also indicates the benefit of frequency selectivity on the harvested power. The gain is particularly obvious in



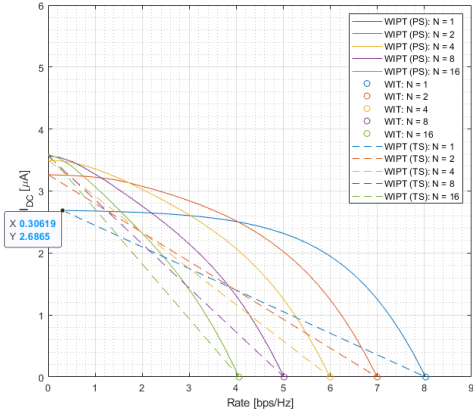
(a) FF: Superposed waveform



(b) FF: No power waveform



(c) FS: Superposed waveform



(d) FS: No power waveform

Figure 4.2: R-E region vs N for FF and FS channels

the low-rate region, where all the power is allocated to the subband with strongest amplitude. Consider the FS channel instance denoted by Figure 4.1(b). Some edge frequencies enjoy a larger gain than the center frequency, whose advantage is exploited when more subbands are used in WIPT. In comparison, the small amplitude at the center frequency accounts for the lower output DC current when $N = 1$ (indicated by the blue curves in 4.2(c) and 4.2(c)). The result is inline with the scaling laws proposed in [11].

Another finding is that without power waveform, the R-E region appears convex such that PS dominates for all N . On the other hand, the R-E region with the superposed waveform by PS is convex for $N = 2, 4$ but concave-convex for $N = 8, 16$. Therefore, the optimal strategy is PS for small N , TS for large N , and a combination of PS and TS for medium N . As illustrated in Figure 4.3, the best curve for medium N consists of two parts. The straight part is achieved by TS between WPT (multisine only and $\rho = 1$) that corresponds to the leftmost point and WIPT (superposed waveform with $0 < \rho < 1$) that corresponds to the tangent point, while the convex part is the contribution of WIPT only. The characteristics of the optimal R-E region comes from the rectifier nonlinearity.

Moreover, the plots over the FS channel suggests that for single-carrier transmission, the modulated waveform outperforms the superposed waveform for WPT. At

a zero-approaching rate, the modulated waveform produces a DC current of 2.69 μA while the superposed waveform only delivers 2.64 μA . The actual current gap is even larger since the former still guarantees a slightly higher rate. On the contrary, the superposed waveform leads to a larger harvested current for $N \geq 2$. It demonstrates that modulation is beneficial in single-carrier transmission but can be detrimental in multi-carrier transmission.

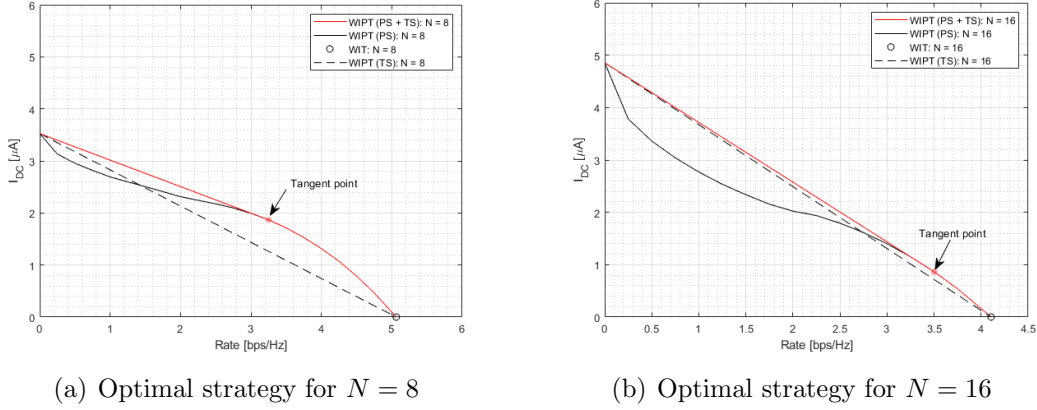


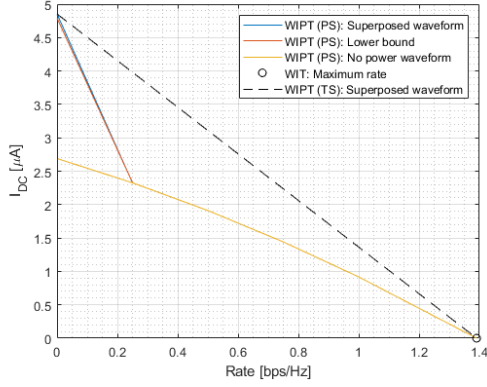
Figure 4.3: Optimal R-E region for FF channel with medium N

One main problem of the results is that the leftmost point of some curves did not start from the y-axis. This is because although a zero rate constraint is employed in WPT, a candidate solution may achieve a nonzero rate. However, if the current gain of the next iteration is smaller than the threshold ε , the algorithm terminates and outputs the existing R-E pair. This phenomenon occurs primarily for small N that produces a lower harvested current (hence smaller gain in each iteration) and low-rate region where the output DC current almost saturated. It can be fixed either by reducing threshold ε or developing an individual function for WPT.

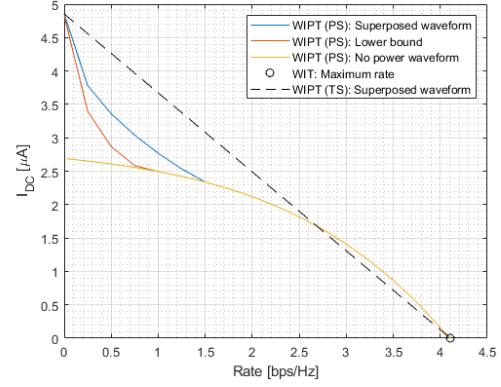
4.1.2 R-E Region vs SNR

Figure 4.4 and 4.5 contrast the performance of the modulated waveform, ideal superposed waveform and its lower bound for $N = 16$ and $\text{SNR} = 10, 20, 30, 40$ dB under the FF and FS channel response in Figure 4.1.

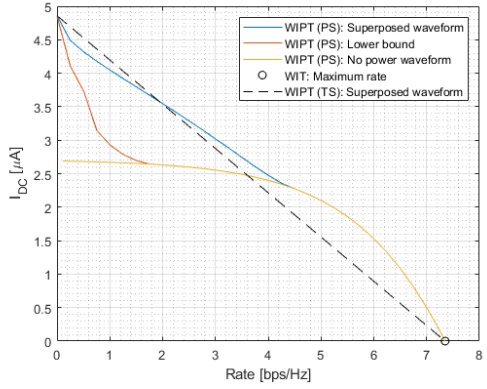
Compared with the modulated signal, the R-E region of the superposed signal is enlarged for both cases with the contribution of the multisine waveform. This phenomenon is especially obvious in the low-rate region where the multisine dominates the transmission. It results from the fact that the nonlinear rectifier favors the deterministic multisine with high PAPR. On the contrary, there are some randomness involved in the modulated waveform that produces fluctuations to the rectifier and leads to some power loss [11]. This phenomenon is in sharp contrast to the argument in [?] that both waveforms are equally suitable for WPT, which is based on the conventional linear harvester model. As shown in Figure 4.4 and 4.5, even with the assumption that the deterministic power waveform creates some interference to the information waveform, the rate loss is compensated by the power gain such that the superposed waveform strictly outperforms the modulated waveform.



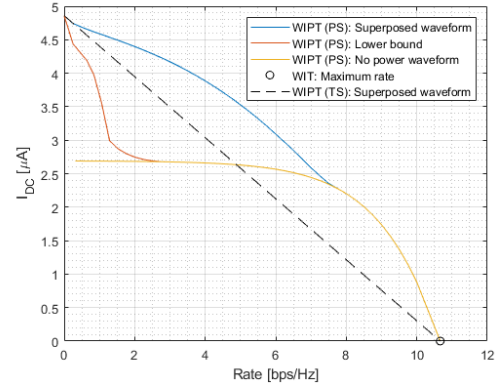
(a) FF: SNR = 10 dB



(b) FF: SNR = 20 dB



(c) FF: SNR = 30 dB



(d) FF: SNR = 40 dB

Figure 4.4: R-E region vs SNR for FF channel

Another observation is that the gap of R-E region between the ideal superposed waveform and its lower bound widens as SNR increases. This is as expected because the rate is dominated by noise at low SNR and by interference at high SNR. For SNR = 10 dB, the interference is far lower than noise even if a large amount of power is allocated to the multisine component, and the curves almost overlap with each other. On the other hand, for a higher SNR as 30 dB, the rate loss by interference increases while the energy benefit of power waveform remains unchanged. To obtain the optimal R-E tradeoff, the transmitter tends to allocate less power to the multisine so that the difference in harvested current increases for a fixed rate. Therefore, the rate boost of deterministic power waveform grows as SNR increases.

It also demonstrates that for the superposed waveform with a sufficiently large N , TS is preferred at low SNR and PS is favored at high SNR, while a combination of TS and PS is generally optimal for medium SNR. On the other hand, the R-E region is strictly convex for the modulated waveform-only transmission due to its inefficiency to boost the harvested energy. It suggests that PS always outperforms TS for no power waveform no matter the SNR. Moreover, the corresponding R-E curve is approximately straight at low SNR but with large curvature at high SNR. The reason is that for a low SNR, the water-filling strategy concentrates the power to the best subband to maximize the rate, and the region boundary is obtained by varying ρ only. In comparison, more subbands are utilized in the transmission as

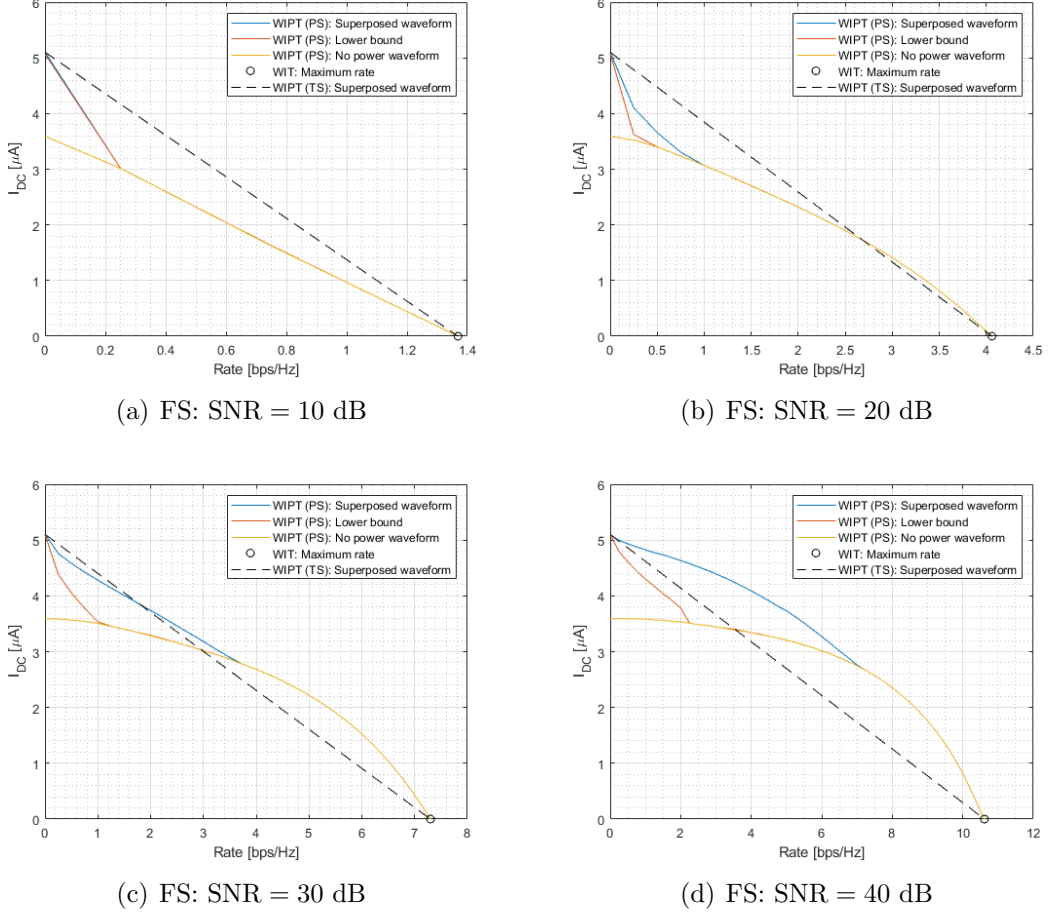


Figure 4.5: R-E region vs SNR for FS channel

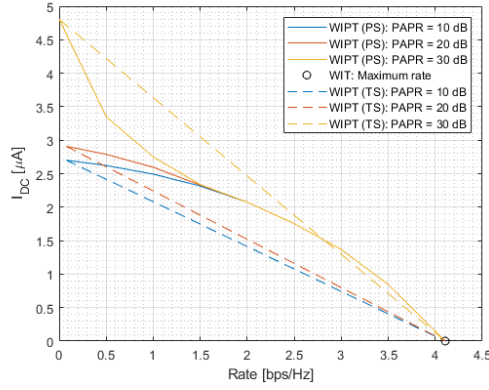
SNR increases. Therefore, only a small portion of power is required to achieve a decent rate such that the output DC current can be maintained at a high level.

A comparison between the results over FF and FS channels emphasizes the benefit of frequency selectivity on the harvested current. The gain is more significant for modulated waveform (around 1 μ A) than superposed waveform (around 0.25 μ A). One possible reason is that the power are concentrated in few subbands such that the number of terms in 2.44 and 2.49 are comparable. In such cases, the impact of channel amplitude on each monomial is more significant on the information waveform and contributes to a larger gain in the harvested current.

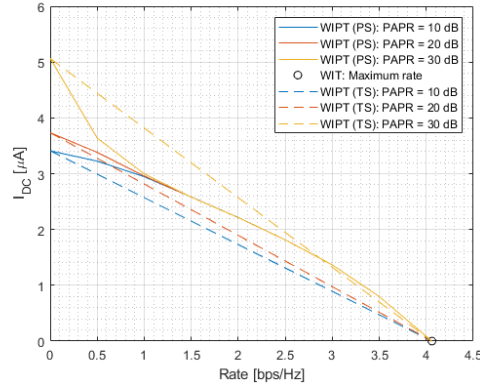
4.1.3 R-E Region vs PAPR

Figure 4.6 investigates the relationship between PAPR and R-E region for $N = 8, 16$ under the FF and FS channel response as in Figure 4.1.

A first observation is that a large enough PAPR is required to fully exploit the power gain of the multisine waveform. For $N = 16$, the R-E region is convex for a PAPR no larger than 20 dB and is concave-convex when it increases to 30 dB. Compare the result with Figure 4.4(b) and 4.5(b), it can be observed that with a small PAPR constraint of 10 dB, the use of multisine waveform is strictly restricted such that the modulated waveform dominates the transmit signal. Hence,



(a) FF: $N = 16$



(b) FS: $N = 16$

Figure 4.6: R-E region vs PAPR for FF channel

the corresponding R-E plot is similar to the result without power waveform. On the contrary, a PAPR of 30 dB is large enough for the optimal performance of the superposed signal in the low-rate region. It can be concluded that the energy benefit of the multisine waveform indeed comes from the high PAPR. In each cycle, the pulse-like peak pushes the rectifier output voltage to a high level which decreases slowly in the rest of the period.

A contrast of the R-E region achieved by $N = 8$ and 16 also suggests a larger N requires higher PAPR for the optimal performance. This verifies the discussion in section 2.2.1 and further suggests that although increasing N can effectively boost the harvested energy, the PAPR constraint may limit the use of a very large N in practice.

4.2 MISO

Next, we switch to the MISO case and investigate the influence of transmit antenna (Tx) on the R-E region. The same multipath channel model is assumed in the simulation. Thanks to the decoupling approach, the predetermined beamforming phases Φ_I^* , Φ_P^* are optimal for MISO and the computational complexity is irrelevant to M . Figure shows the result over an instance FF channel for $M = 2, 3$ and $N = 4$.

A first observation is that the concavity-convexity appears for $N = 4$ for the

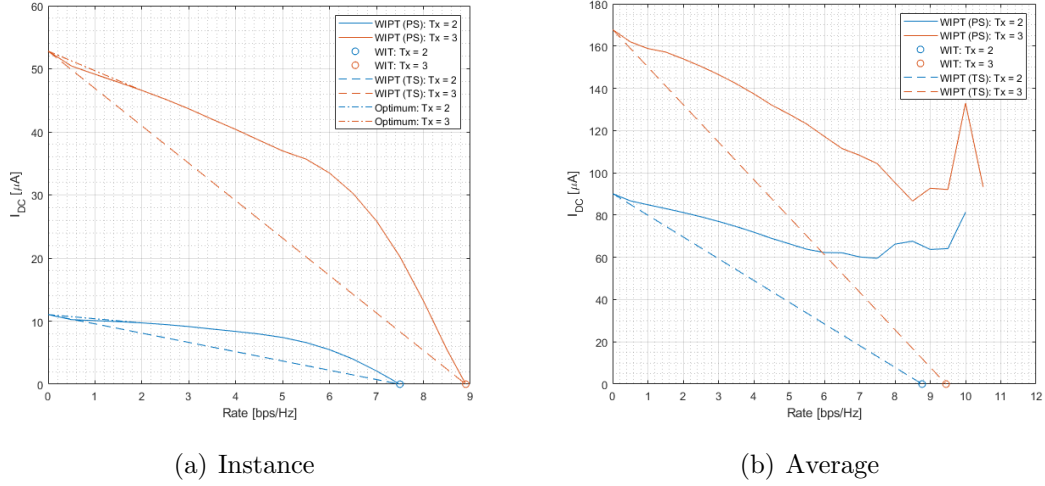


Figure 4.7: R-E region vs M over FF channel: an instance and the average over 100 realizations

MISO systems, in contrast to $N = 8$ in the SISO case. It suggests that a large M can further boost the energy benefit by multisine waveform. The reason is that increasing M essentially produces more subchannels for transmission such that the coupled terms contributing to the harvested current are amplified. Also, a smaller N is needed to achieve a certain output current level and the transmitted waveform is with a lower PAPR. Hence, increasing M can be a possible solution for PAPR-constrained devices. Moreover, a combination of TS (between WPT and WIPT) at low rate and PS at high rate guarantees the optimal R-E region as a convex hull.

To eliminate the influence of channel randomness, we investigate the R-E tradeoff for 100 FF channels with $N = 4$. However, the averaged plot of Figure 4.7(b) is not a good representation for the general performance. At the low-rate region ($R \leq 5$ bps/Hz), the curves showed some concavity as expected. This is because the capacity of most channels can satisfy such a low rate constraint and guarantee valid R-E pairs that contributes to the averaged points. Nevertheless, as the rate constraint increases, only strong channels can support WIPT while those weak channels are abandoned. For instance, if the per-subband rate requirement is 10 bps/Hz but the capacity of 90 % channels are below this value, then only 10 % channels will be considered in the averaging. Therefore, the high-rate region is indeed dominated by some strong channels. Increasing the number of channels may mitigate the phenomenon to some extent, but a better representation is required to avoid channel randomness and characterize the general R-E region.

Figure 4.8 shows the Cumulative Distribution Function (CDF) of maximum rate and DC current that correspond to WIT and WPT respectively. It is less interesting for WIPT since the variation trend of the R-E tradeoff is not presented.

4.3 MIMO

We then explore the impact of receive antenna (Rx) and subband on the R-E region for MIMO system with $M = 2$ under a typical FF channel. The dominant eigenvalue of each subband is shown in Figure 4.9.

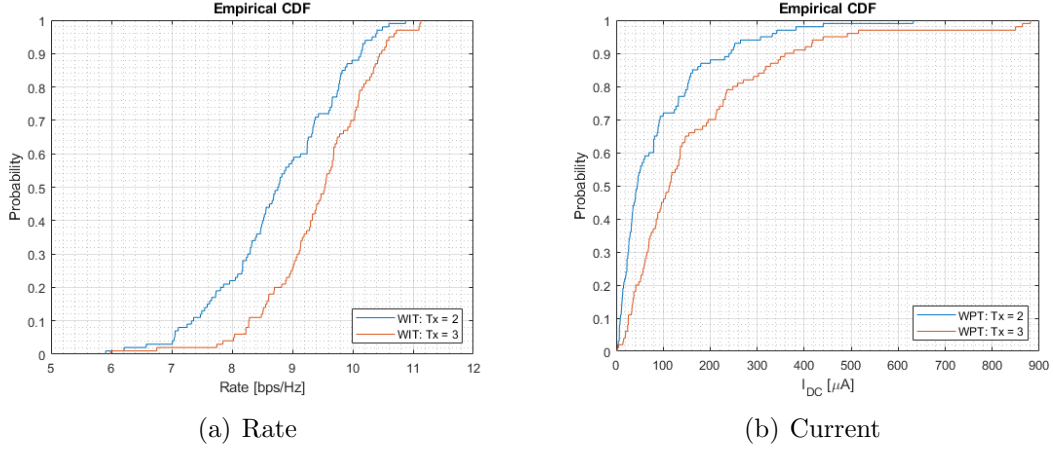


Figure 4.8: Rate and current CDF vs M for MISO FF channels

As illustrated in Figure 4.8 a contrast between $U = 2$ and 3 suggests that increasing R_x may boost the rate and energy simultaneously, thanks to the multiplexing gain of MIMO. The reason is that for a fixed $M = 2$, increasing U from 2 to 3 provides no extra streams for transmission but leads to a larger eigenvalue of channel matrix, which benefits the R-E region by increasing the effective subband amplitude.

On the other hand, a large N amplifies the harvested power thanks to the rectifier nonlinearity. It can be observed that the R-E curves begin to show some concavity-convexity for $N = 4$, which was first observed for $N = 8$ in SISO channels. A possible reason is that with the aforementioned configuration, each subchannel has 2 virtual streams so that the equivalent subband is indeed $4 \times 2 = 8$. Therefore, MIMO demonstrates a twofold benefit in rate and energy, which requires a smaller N to achieve a certain output power level and is more suitable for low-PAPR systems.

Despite as expected, the conclusions require more evidence since only one specific channel is investigated in the simulation. An averaged result over numerous realizations as in section 4.3 can be more persuasive.

The main problem of Figure 4.10 is that the rightmost points of the R-E curves do not reach the x-axis. It results from the discrete rate constraints employed in the simulation. With a step of 1 bps/Hz, the points tend to locate near the integer rates. For instance, the plot corresponding to $U = 2$ and $N = 4$ terminates at a rate of 6 bps/Hz with an output current of 22 μ A, since proposed PS-WIPT strategy cannot achieve the next rate milestone of 7 bps/Hz. The reason is that the suboptimal phases Φ'_P, Φ'_I are determined before the optimization so that the algorithm cannot reach the channel capacity corresponding to WIT. In other words, the GP approach is suboptimal for MIMO systems.

For a fixed M and U , a good R-E tradeoff can be obtained by a combination of the following strategies. In the low-rate region, PS-WIPT is optimal for small N and TS between WPT and WIPT is optimal for large N . As rate requirement increases, PS-WIPT can generally guarantee a decent performance on both rate and energy. When the rate constraint is high, TS between WIT and WIPT is the best strategy to enjoy the benefit of multisine and avoid the rate loss of suboptimal phases.

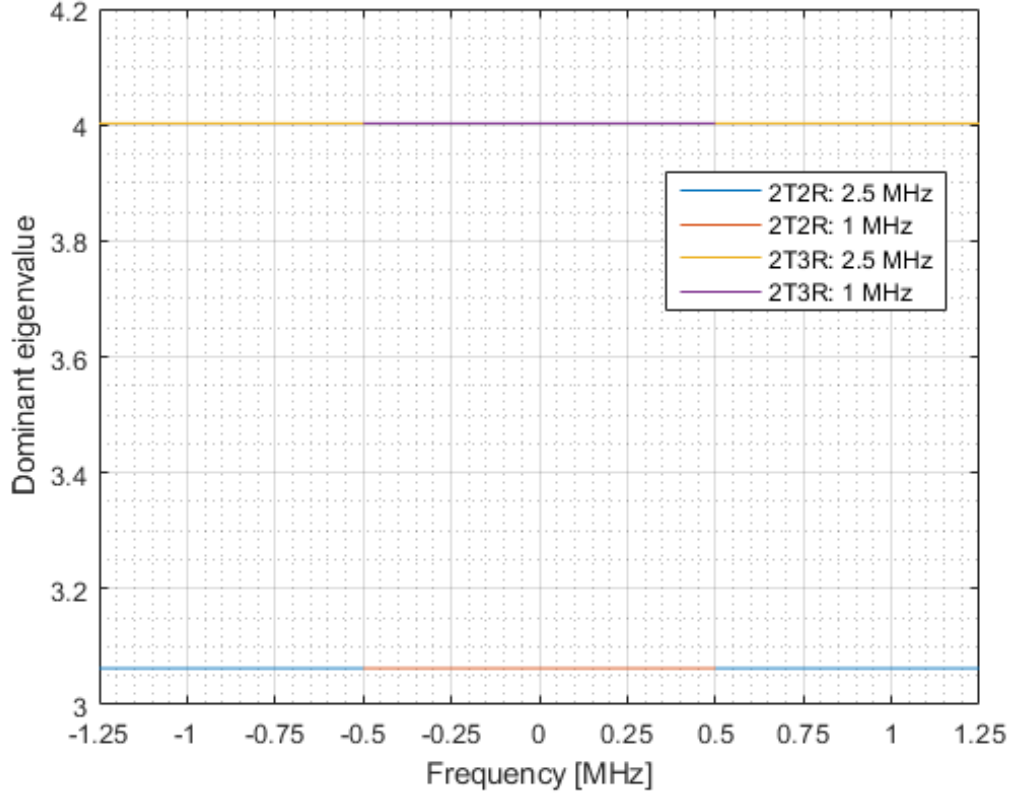
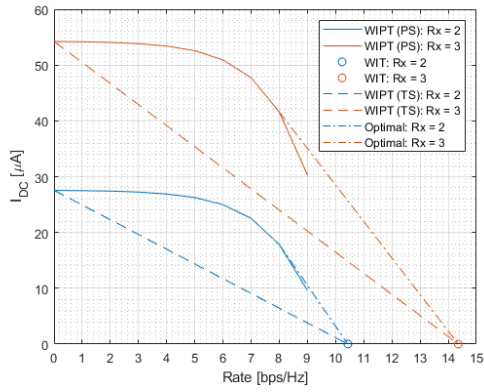
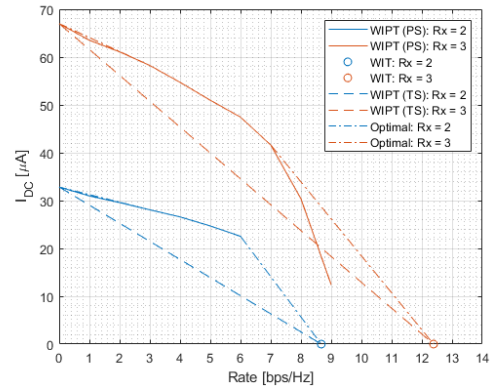


Figure 4.9: Frequency response of the MIMO FF channel



(a) FF: $N = 2$



(b) FF: $N = 4$

Figure 4.10: R-E region vs N and U for MIMO FF channels

Bibliography

- [1] B. Clerckx, A. Costanzo, A. Georgiadis, and N. Borges Carvalho, “Toward 1G Mobile Power Networks: RF, Signal, and System Designs to Make Smart Objects Autonomous,” *IEEE Microwave Magazine*, vol. 19, no. 6, pp. 69–82, 2018.
- [2] M. S. Trotter, J. D. Griffin, and G. D. Durgin, “Power-optimized waveforms for improving the range and reliability of RFID systems,” *2009 IEEE International Conference on RFID, RFID 2009*, pp. 80–87, 2009.
- [3] B. Clerckx, R. Zhang, R. Schober, D. W. K. Ng, D. I. Kim, and H. V. Poor, “Fundamentals of wireless information and power transfer: From RF energy harvester models to signal and system designs,” *IEEE Journal on Selected Areas in Communications*, vol. 37, no. 1, pp. 4–33, 2019.
- [4] D. W. K. Ng, T. Q. Duong, C. Zhong, and R. Schober, *Wireless Information and Power Transfer: Theory and Practice*. Wiley-IEEE Press, 2019.
- [5] L. R. Varshney, “Transporting Information and Energy Simultaneously,” *IEEE International Symposium on Information Theory - Proceedings*, pp. 1612–1616, 2008.
- [6] P. Grover and A. Sahai, “Shannon meets tesla: Wireless information and power transfer,” *IEEE International Symposium on Information Theory - Proceedings*, pp. 2363–2367, 2010.
- [7] R. Zhang and C. K. Ho, “MIMO broadcasting for simultaneous wireless information and power transfer,” *IEEE Transactions on Wireless Communications*, vol. 12, no. 5, pp. 1989–2001, 2013.
- [8] X. Zhou, R. Zhang, and C. K. Ho, “Wireless information and power transfer in multiuser OFDM systems,” *GLOBECOM - IEEE Global Telecommunications Conference*, vol. 13, no. 4, pp. 4092–4097, 2013.
- [9] L. Liu, R. Zhang, and K. C. Chua, “Wireless information and power transfer: A dynamic power splitting approach,” *IEEE Transactions on Communications*, vol. 61, no. 9, pp. 3990–4001, 2013.
- [10] B. Clerckx and E. Bayguzina, “Waveform Design for Wireless Power Transfer,” *IEEE Transactions on Signal Processing*, vol. 64, no. 23, pp. 6313–6328, 2016.
- [11] B. Clerckx, “Wireless Information and Power Transfer: Nonlinearity, Waveform Design, and Rate-Energy Tradeoff,” *IEEE Transactions on Signal Processing*, vol. 66, no. 4, pp. 847–862, 2018.

- [12] M. Varasteh, E. Piovano, and B. Clerckx, "A Learning Approach To Wireless Information and Power Transfer Signal and System Design," pp. 4534–4538, 2018. [Online]. Available: <http://arxiv.org/abs/1810.12152>
- [13] S. Y. Hui, W. Zhong, and C. K. Lee, "A critical review of recent progress in mid-range wireless power transfer," *IEEE Transactions on Power Electronics*, vol. 29, no. 9, pp. 4500–4511, 2014.
- [14] E. Boshkovska, D. W. K. Ng, N. Zlatanov, and R. Schober, "Practical non-linear energy harvesting model and resource allocation for SWIPT systems," *IEEE Communications Letters*, vol. 19, no. 12, pp. 2082–2085, 2015.
- [15] Y. Zeng, B. Clerckx, and R. Zhang, "Communications and Signals Design for Wireless Power Transmission," *IEEE Transactions on Communications*, vol. 65, no. 5, pp. 2264–2290, 2017.
- [16] A. S. Boaventura and N. B. Carvalho, "Maximizing DC power in energy harvesting circuits using multisine excitation," *IEEE MTT-S International Microwave Symposium Digest*, vol. 1, no. 1, pp. 1–4, 2011.
- [17] T. Takahashi, T. Mizuno, M. Sawa, T. Sasaki, T. Takahashi, and N. Shinohara, "Development of phased array for high accurate microwave power transmission," *2011 IEEE MTT-S International Microwave Workshop Series on Innovative Wireless Power Transmission: Technologies, Systems, and Applications, IMWS-IWPT 2011 - Proceedings*, pp. 157–160, 2011.
- [18] Y. S. Chen and C. W. Chiu, "Maximum achievable power conversion efficiency obtained through an optimized rectenna structure for RF energy harvesting," *IEEE Transactions on Antennas and Propagation*, vol. 65, no. 5, pp. 2305–2317, 2017.
- [19] A. Collado and A. Georgiadis, "Optimal waveforms for efficient wireless power transmission," *IEEE Microwave and Wireless Components Letters*, vol. 24, no. 5, pp. 354–356, 2014.
- [20] A. Boaventura, D. Belo, R. Fernandes, A. Collado, A. Georgiadis, and N. B. Carvalho, "Boosting the Efficiency: Unconventional Waveform Design for Efficient Wireless Power Transfer," *IEEE Microwave Magazine*, vol. 16, no. 3, pp. 87–96, 2015.
- [21] A. Dolgov, R. Zane, and Z. Popovic, "Power management system for online low power RF energy harvesting optimization," *IEEE Transactions on Circuits and Systems I: Regular Papers*, vol. 57, no. 7, pp. 1802–1811, 2010.
- [22] J. A. G. Akkermans, M. C. Van Beurden, G. J. N. Doodeman, and H. J. Visser, "Analytical models for low-power rectenna design," *IEEE Antennas and Wireless Propagation Letters*, vol. 4, no. 1, pp. 187–190, 2005.
- [23] A. Boaventura, A. Collado, N. B. Carvalho, and A. Georgiadis, "Optimum behavior: Wireless power transmission system design through behavioral models and efficient synthesis techniques," *IEEE Microwave Magazine*, vol. 14, no. 2, pp. 26–35, 2013.

- [24] M. Stoopman, S. Keyrouz, H. J. Visser, K. Philips, and W. A. Serdijn, "Co-design of a CMOS rectifier and small loop antenna for highly sensitive RF energy harvesters," *IEEE Journal of Solid-State Circuits*, vol. 49, no. 3, pp. 622–634, 2014.
- [25] C. R. Valenta and G. D. Durgin, "Harvesting wireless power: Survey of energy-harvester conversion efficiency in far-field, wireless power transfer systems," *IEEE Microwave Magazine*, vol. 15, no. 4, pp. 108–120, 2014.
- [26] A. Georgiadis, A. Collado, S. Via, and C. Meneses, "Flexible hybrid solar/EM energy harvester for autonomous sensors," *IEEE MTT-S International Microwave Symposium Digest*, pp. 1–4, 2011.
- [27] A. Collado and A. Georgiadis, "Conformal hybrid solar and electromagnetic (EM) energy harvesting rectenna," *IEEE Transactions on Circuits and Systems I: Regular Papers*, vol. 60, no. 8, pp. 2225–2234, 2013.
- [28] J. O. McSpadden, L. Fan, and K. Chang, "Design and Experiments of a High-Conversion-Efficiency 5.8-GHz Rectenna," *IEEE Transactions on Microwave Theory and Techniques*, vol. 46, no. 12, pp. 2053–2060, 1998.
- [29] J. Guo and X. Zhu, "An improved analytical model for RF-DC conversion efficiency in microwave rectifiers," *IEEE MTT-S International Microwave Symposium Digest*, pp. 1–3, 2012.
- [30] A. Costanzo and D. Masotti, "Smart Solutions in Smart Spaces: Getting the Most from Far-Field Wireless Power Transfer," *IEEE Microwave Magazine*, vol. 17, no. 5, pp. 30–45, 2016.
- [31] H. Sun, Z. Zhong, and Y. X. Guo, "An adaptive reconfigurable rectifier for wireless power transmission," *IEEE Microwave and Wireless Components Letters*, vol. 23, no. 9, pp. 492–494, 2013.
- [32] B. Strassner and K. Chang, "Microwave power transmission: Historical milestones and system components," *Proceedings of the IEEE*, vol. 101, no. 6, pp. 1379–1396, 2013.
- [33] B. Clerckx and E. Bayguzina, "Low-Complexity Adaptive Multisine Waveform Design for Wireless Power Transfer," *IEEE Antennas and Wireless Propagation Letters*, vol. 16, no. 1, pp. 2207–2210, 2017.
- [34] J.-p. Curty, N. Joehl, C. Dehollain, and M. J. Declercq, "A Model for Mu-Power Rectifier Analysis and Design," *Technology*, vol. 52, no. 12, pp. 2771–2779, 2005. [Online]. Available: [#](http://scholar.google.com/scholar?hl=en&btnG=Search&q=intitle:A+Model+for+-Power+Rectifier+Analysis+and+Design)0
- [35] M. Varasteh, B. Rassouli, and B. Clerckx, "On Capacity-Achieving Distributions for Complex AWGN Channels Under Nonlinear Power Constraints and their Applications to SWIPT," vol. 2017, 2017. [Online]. Available: <http://arxiv.org/abs/1712.01226>

- [36] S. Boyd, S. J. Kim, L. Vandenberghe, and A. Hassibi, “A tutorial on geometric programming,” *Optimization and Engineering*, vol. 8, no. 1, pp. 67–127, 2007.
- [37] M. Chiang, *Geometric Programming for communication systems*, 2005, vol. 2, no. 1-2.
- [38] B. R. Marks and G. P. Wright, “Technical Note—A General Inner Approximation Algorithm for Nonconvex Mathematical Programs,” *Operations Research*, vol. 26, no. 4, pp. 681–683, 1978.
- [39] J. Medbo and P. Schramm, “Channel Models for Hiperlan/2 in Different Indoor Scenarios,” *ETSI EP BRAN*, vol. 3ERI085B, 1998.